Mantle-driven, climatically modulated landscape evolution in Southern Patagonia

Victoria M. Fernandes[1*], Andreas Ruby[1], Fergus McNab[1], Hella Wittmann[1], Andrew D. Wickert[1,2], Lennart Grimm[1] & Taylor Schildgen[1,3]

[1] GFZ Helmholtz Centre for Geosciences, 14473 Potsdam, Germany

[2] St. Anthony Falls Laboratory and Department of Earth & Environmental Sciences, University of Minnesota, 55455 Minneapolis, USA

[3] Institute for Geosciences, University of Potsdam, 14476 Potsdam, Germany

*milanez@gfz.de

Mantle-driven, climatically modulated landscape evolution in Southern Patagonia

Victoria M. Fernandes[1*], Andreas Ruby[1], Fergus M^c^Nab[1], Hella Wittmann[1], Andrew D. Wickert[1,2], Lennart Grimm[1] & Taylor Schildgen[1,3]

[1] GFZ Helmholtz Centre for Geosciences, 14473 Potsdam, Germany

[2] St. Anthony Falls Laboratory and Department of Earth & Environmental Sciences, University of Minnesota, 55455 Minneapolis, USA

[3] Institute for Geosciences, University of Potsdam, 14476 Potsdam, Germany

*milanez@gfz.de

ABSTRACT

We explore the relative importance of tectonic, geodynamic and surface processes in driving landscape evolution in Argentine Patagonia using 64 new ^{10}Be exposure ages of fluvial terraces preserved over >250 km along the Shehuén and Santa Cruz rivers (50ºS). Terrace ages range from 33 ka to 1.5 Ma, and coincide with Patagonian glaciations. We demonstrate that landscapes can respond directly to changes in climate forcing driven by the Mid-Pleistocene Transition: our results reveal a transition to 100-ky terrace periodicity, and a transient phase of accelerated incision starting at ~1 Ma. A regionally uniform incision rate of 130–180 m Ma^{-1} since 1 Ma suggests uplift linked toasthenospheric heating in the Patagonian slab window, while transient accelerated incision suggests convective instabilities in a low-viscosity mantle. We establish a temporal link between climate oscillations, fluvial incision, and mantle-driven epeirogenic uplift.

INTRODUCTION

Landscapes are the product of complex interactions between climate, tectonic, and surface processes operating over multiple spatial and temporal scales. Disentangling their relative contributions is challenging; tectonic and climatic signals tend to mask one another, and isolating long-term geodynamic drivers requires data that span sufficiently long spatial and temporal scales.

The Southern Patagonian steppe uniquely combines an absence of crustal deformation (Lagabrielle et al. 2004), pronounced geodynamic influences (Dávila & Lithgow-Bertelloni, 2013), and prominent glaciation (Mercer, 1983), which occur within the semi-arid rain shadow of the Andes (~300 mm a^{-1}; Blisniuk et al., 2005). This setting creates an ideal framework for isolating geomorphic responses to climate and geodynamics, where geomorphic features are preserved without the confounding overprint of orogenic activity.

Since 14 Ma, the subducting Chile Triple Junction has migrated north from 54ºS to 46ºS, progressively opening a slab window beneath South America (Fig. 1A; Lagabrielle et al., 2004), influencing regional magmatism, uplift and landscape evolution (Gorring et al., 1997, Guillaume et al., 2009, Tobal et al., 2021). East of the thrust front, the foreland has been tectonically quiescent since the Late Miocene (Lagabrielle et al., 2004). Epeirogenic uplift along the Patagonian coastline (Pedoja et al., 2011) has been attributed to dynamic topography (Guillaume et al., 2009, Dávila & Lithgow-Bertelloni, 2013, Hollyday et al., 2023) or an isostatic response to lithospheric thinning (Ávila & Dávila, 2020), consistent with observed thin lithosphere, hot asthenosphere and low mantle viscosity (Mark et al., 2022).

The record of epeirogenic uplift in Patagonia is not temporally continuous. Coastal outcrops of intertidal deposits constrain paleo-sea level and vertical motions since the Early Pliocene (4.69–5.23 Ma; Hollyday et al., 2023), while marine terraces record uplift from MIS 11 (424 ka; Pedoja et al.,

2011) to the Late Holocene (3000 yr BP; Rubio-Sandoval et al., 2024). The morphology of fluvial terraces in Patagonia has been used to infer regional-scale mantle-driven uplift and foreland surface tilting, but its timing is poorly resolved (Guillaume et al., 2009, Tobal et al., 2021). Records of vertical motions of the Patagonian steppe that span this temporal gap and extend inland are thus critical for understanding the evolution of the slab window and the landscape above it.

Glacial activity, comprising waxing and waning of the Patagonian ice sheet in response to orbitally-driven climate cycles, is also an important driver of landscape change in the region (Schellmann, 2000). Shorter mantle relaxation times due to low-viscosity mantle within the slab window enhance glacio-isostatic responses to ice-volume fluctuations (Dietrich et al., 2010). Regional glacial chronologies (Mercer, 1983, Ton-That et al., 1999, Rabassa et al., 2005, Clague et al., 2020, Hein et al., 2011; Tobal et al., 2021; see Supplemental Material[1]) form a near-continuous record since ~7 Ma. Critically, this record spans the Mid-Pleistocene Transition (MPT, 1.2–0.8 Ma), a time when a shift in the dominant periodicity of Earth's climate significantly impacted landscape evolution, particularly in regions sensitive to glacial dynamics (Valla et al., 2011).

Enhanced river incision associated with this climatic shift has been recognized in the Central Andes (Pingel et al., 2019) and Patagonia (Lagabrielle et al. 2007, Tobal et al., 2021). While 100-ky cyclicity of fluvial terrace abandonment has been observed in Andean rivers (Orr et al., 2024), sparse absolute chronologies of Patagonian terraces have led to only speculation on the role of the MPT in enhancing fluvial and glacial incision (Tobal et al., 2021) and preclude assessment of the relative contributions of climate and geodynamics on landscape evolution.

By mapping and dating fluvial terraces along the Santa Cruz and Shehuén rivers (50ºS), we establish a detailed Pleistocene history of river incision. We then explore the extent to which regional climate versus deep-Earth processes may have contributed to river incision.

Study Area

Fluvial terraces extend >250 km along the Santa Cruz and Shehuén rivers (Fig. 1B). Water and sediment are supplied by the San Martín, Viedma and Argentino lakes (49–50ºS), which in turn are fed by meltwater from the Southern Patagonian Icefield. Fill terraces comprise coarse gravel and cobbles in a sandy matrix, occasionally overlying outcrops of marine-derived Oligo-Miocene bedrock (see Sup. Mat.).

Upstream, several terraces coincide with terminal moraines, pointing to a glacial origin (see Sup. Mat.). The oldest cosmogenic ^{10}Be dated moraines in the Argentino-Viedma-San Martín valleys are 245 ka (Romero et al., 2024), although older moraine sequences are mapped (Schellmann, 2000). Local interbedded till and dated basalt flows constrain Early Pleistocene glaciations to 1.08 Ma and older (Singer et al., 2004).

In the Santa Cruz valley, stacked basalt flows at Condor Cliffs (50.2ºS, 70.9ºW) range from 3.25±0.08 Ma at the base (Clague et al., 2020) to 1.7±0.5 Ma at the top (Schnellmann, 2000). In the upper Shehuén valley, basalt flows are dated between 3.1±0.15 and 2.13±0.09 Ma (Wenzens, 2000, Clague et al., 2020). In both valleys, these flows are, in places, overlain and underlain by till, or preserve remnant terrace fill above them. The ages and distribution of basalt flows show that the paleo-Santa Cruz River flowed in a valley floor 100 m above its present level between 3.2–1.7 Ma. The valley subsequently experienced multiple cycles of fill and incision, producing the terraces observed today.

METHODS

We mapped basalt flows using geological maps, satellite imagery and field observations. Locations of glacial moraine deposits were compiled from existing geomorphic maps and additional field mapping. We mapped fluvial terraces using TanDEM-X (12-m resolution) digital elevation data, complemented by 1:250,000 scale geological maps and other works, and correlated terrace patches based on elevation and stratigraphic relationships with basalt flows (see Sup. Mat.). Terrace paleo-profiles were generated by projecting elevations for each terrace level to a valley center-line (see Sup. Mat. for details).

To determine terrace abandonment ages, we measured *in situ* produced cosmogenic ^{10}Be from 53 cobble and 11 amalgamated pebble samples (N=100 for each sample, 1–3 cm diameter) from terrace surfaces. To minimize the influence of erosion or burial on exposure ages, sample locations were chosen tens of meters from the closest terrace edge, gully or alluvial fan. All cobbles collected were smooth and well rounded, suggesting minimal post-transport erosion of the cobble itself. Patches of surface loess raise the possibility of intermittent burial/erosion. We also collected a 4-sample depth profile from the lowest terrace of the Shehuén River, comprising amalgamated pebble samples (N>100, 1–3 cm diameter) from the surface to 1.5 m depth, with each sample collected within a 10 cm depth interval. Details of sampling locations, preparation, analysis, exposure-age calculation, and age interpretation are provided in the Supplemental Material.

RESULTS

We identify 6 unique terrace levels in the Santa Cruz valley, 8 in the Shehuén, and 7 shared by both valleys. The San Fernando terrace (Figs. 1 and 2) is continuous along both rivers, providing a regional stratigraphic marker. Field observations confirm the San Fernando terrace stratigraphically overlies the youngest basalt at Condor Cliffs, constraining its age to <1.7± 0.5 Ma (Strelin & Malagnino, 2009, Clague et al., 2020; Sup. Mat.). In their downstream reaches (>100 km), terraces are sub-parallel, with slopes similar to the modern floodplain (Figs. 1C & D).

Depth profile modeling (Fig. 3A & B) of the youngest terrace in the Shehuén valley yields an exposure age of $33.3^{+3.6}_{-7.1}$ ka and an inherited ^{10}Be concentration of $6.4^{+2.1}_{-3.9}$ x10^4 at g^{-1}. Individual cobble and amalgamated pebble exposure ages from each terrace level were combined to determine the age of 5 terrace levels in the Santa Cruz and 7 in the Shehuén valley (Fig. 2). Terrace ages range from 33 ka to 1.5 Ma. Ages grouped by terrace level form statistically coherent and stratigraphically consistent age populations (i.e., increase with elevation), especially when outliers are removed (see Sup. Mat.). We interpret old and young outliers to reflect anomalous inheritance and erosion, respectively (cf. Hein et al., 2011; Tobal et al., 2021). The Las Lascas terrace age is poorly constrained, but is at most 1510^{+82}_{-82} ka. The San Fernando terrace has an age of 1028^{+76}_{-103} ka, with subsequent terraces formed within 100 kyr (Punta Piedra II = 1008^{+58}_{-58} ka, Punta Piedra I = 988^{+61}_{-114} ka). Lower terraces form in ~100 kyr intervals (El Mosquito = 928^{+49}_{-86} ka, Lucero = 868^{+44}_{-62} ka, Indice = 781^{+47}_{-196} ka), with a 400 kyr gap to the following levels, which also form in ~100 kyr intervals (La Victoria = 380^{+26}_{-118} ka, Chuñi Aike = 240^{+19}_{-70} ka, Urbana = 127^{+13}_{-22} ka, El Amor = $33.3^{+3.6}_{-7.1}$ ka).

Our terrace mapping (see Sup. Mat.) and interpreted ages reveal a similar timing and pattern of incision along the Shehuén and Santa Cruz valleys (Fig. 3C & D). At ~1 Ma, both valleys experienced rapid incision (660 to 2250 m Ma^{-1}), with a subsequent reduction for the Shehuén to 293 m Ma^{-1} between ~1000–800 ka. Starting at ~900–800 ka, incision rates dropped substantially (24 to 49 m Ma^{-1}), then increased again after 400 ka (88 to 181 m Ma^{-1}).

DISCUSSION & CONCLUSIONS

Climate modulation of incision

We interpret that the San Fernando (1028 ka), Punta Piedra II (1008 ka) and Punta Piedra I (988 ka) terrace levels formed in response to multiple glaciations associated with the Great Patagonian Glaciation (GPG, Fig. 4, Mercer, 1983; Griffing et al., 2022). Additional undated terrace levels that lie between these must have formed between 1028–1008 ka in the Shehuén (Bagual I and II; Fig. 3C), and 1028–928 ka in the Santa Cruz valley (Fig. 3D).

Post-GPG terraces can be correlated with major Patagonian glaciations during global glacial periods (MIS 24, 22, 20, 10, 8, 6 and 3; Fig. 4, see Sup. Mat.). The terrace chronology spans the MPT, and shows a transition from shorter periodicity (1028, 1008, 988 ka) to ~100-kyr periodicity (928, 868, 781, 380, 240, 127, 33 ka), suggesting that the landscape is responding to cyclic climate forcing, likely through variations in the sediment-to-water discharge ratio (McNab et al., 2023).

Accelerated incision at ~1 Ma, as observed in this study, has also been observed in glacial landscapes of Southern Patagonia (Torres del Paine, 51ºS; Muller et al., 2024a). A change in precipitation across the foreland cannot explain the accelerated incision, due to low rainfall since the Miocene (Blisniuk et al., 2005). Greater ice accumulation during the GPG, coinciding with the MPT, may have enhanced glacial erosion, and increased meltwater discharge during post-GPG deglaciations may have incised fluvial valleys downstream (Kaplan et al., 2009, Clague et al., 2020).

The observed temporal gap in the terrace record must be an artifact of preservation, since a continuous record of glaciations exists for MIS 20–10 in Northern Patagonia (Fig. 4). Preservation of terrace sequences requires net incision. Since downstream terrace slopes are sub-parallel to the current channel, and the incision history of the Santa Cruz–Shehuén Rivers is similar to that of the Deseado

River, 47°S (Tobal et al., 2021), it is likely that external factors modulating incision rate control terrace preservation.

Glacio-isostatic adjustment (GIA) in response to variable glacial loading from the Patagonian ice sheet offers a plausible mechanism that modulates incision on such scales. Uplift of a peripheral bulge can significantly alter fluvial incision (e.g., Pico et al., 2019). However, the low elastic thickness of the Patagonian lithosphere limits terrace formation by this mechanism to <200 km from the main ice load (Dietrich et al., 2010), which may only explain steepened slopes at the upstream ends of the terraces (<50 km; Fig. 1C & D). GIA models suggest a maximum surface tilting of ~18 m across the entire river system over the past 5 Myr (Hollyday et al., 2023), which is insufficient to explain the incision-rate variations.

Mantle drivers of landscape evolution

Fluvial incision rates derived from post-MIS 11 terraces of the Shehuén and Santa Cruz Rivers (181–88 m Ma^{-1}) are indistinguishable from long-term rates (184–106 m Ma^{-1} since ~1 Ma). Our terrace-derived incision rates are similar to other regional estimates (Figs. 3B & C): 138 m Ma^{-1} from 1.19 Ma incised basalt flows at Meseta Lago Buenos Aires (Lagabrielle et al. 2007), 135 m Ma^{-1} from ^{10}Be dated terraces of the Deseado River, 46.5ºS (Tobal et al., 2021), and 100–200 m Ma^{-1} regional (42–55ºS) coastal uplift rates since MIS 11 (Pedoja et al., 2011). The uniformity in uplift and incision rates from the proglacial lakes to the Atlantic Ocean (>300 km), spanning 9º of latitude (~1000 km), supports earlier inferences that regional uplift and incision are responses to mantle convection.

Geodynamic models of residual topography in the Patagonian foreland suggest that lithospheric thinning has influenced long-term uplift, but only in the proximal foreland (Ávila & Dávila, 2020). Thermo-mechanical modeling of satellite-derived uplift rates suggest excess asthenospheric temperatures of 100–200ºC in the slab window (Muller et al., 2024b), which could also generate regional uplift. If this excess temperature is regionally distributed, it could generate up to 1.4 km of isostatic uplift (see Sup. Mat.). If emplacement of hot, buoyant mantle material occurred over timescales of slab window opening (~10 Ma), uplift rates would be similar to our observed long-term incision rates (~140 m Ma^{-1}). While these mechanisms can explain long-term incision of the Santa Cruz and Shehuén Rivers, they cannot explain the sub-million-year incision rate variations.

We suggest that both mean incision rates and transient incision accelerations reflect dynamic uplift resulting from convection in a low viscosity mantle. Dynamic uplift is often modeled on timescales of 5–10 Ma, so that only vertical motions on length-scales >10^3 km are resolved. For example, predictions from mantle convection models suggest ~5 m of uplift across S. Patagonia over the last 5–10 Ma (Rovere et al., 2020), two orders of magnitude lower than our observed long-term incision rates. Finer resolution models suggest that small-scale dynamic uplift (~500 km wavelength) can vary on timescales of 1–10 Myr, and that convective instabilities can create static waves of dynamic topography of the order 10^2 m (Arnould et al., 2018). Since low mantle viscosity promotes small-scale convection, with mantle viscosities as low as 10^{18} Pa s within the slab window (Mark et al. 2022), it is possible that the short-term variations in incision rate reflect mantle convection instabilities on a sub-million-year timescale.

In summary, our fluvial terrace chronology reveals a glacial cycle transition into 100-kyr periodicity, and an accelerated phase of incision since the onset of the MPT and the demise of the GPG. Regional patterns of mantle-driven uplift previously observed along the Patagonian coast extend inland, preserving terraces. Sub-million-year variations in incision rate may record convective instabilities in hot, low viscosity asthenospheric mantle within the slab window.

ACKNOWLEDGEMENTS

This work was supported by ERC Consolidator Grant 863490 GyroSCoPe awarded to TS, and an Alexander von Humboldt Foundation research Fellowship to ADW.

[1]Supplemental Material. Text: 1. Field photographs (10). 2. References for mapping moraines, basalt flows and fluvial terraces. 3. Extraction of terrace paleo-profiles. 4. Depth profile modeling methods and parameters. 5. Terrace sample collection and exposure age calculation (CREp). 6. Terrace age interpretation. 7. Patagonian glacial chronology and correlation with terrace ages. 8. Uplift calculations for heated asthenosphere. Supplemental Dataset 1: Sample information and data for reproducing ^{10}Be exposure ages. Supplemental Dataset 2: Terrace longitudinal profile data (Figure 1C and 1D).

Figure 1. (A) Regional map showing evolution of the slab window (solid, dashed black lines), maximum extent of Patagonian ice during GPG (white dashed line), and study area (red box). (B) Santa Cruz and Shehuén Rivers, mapped terraces, basalt flows and moraines. (C) Paleo-profiles of the Shehuén and (D) Santa Cruz terraces.

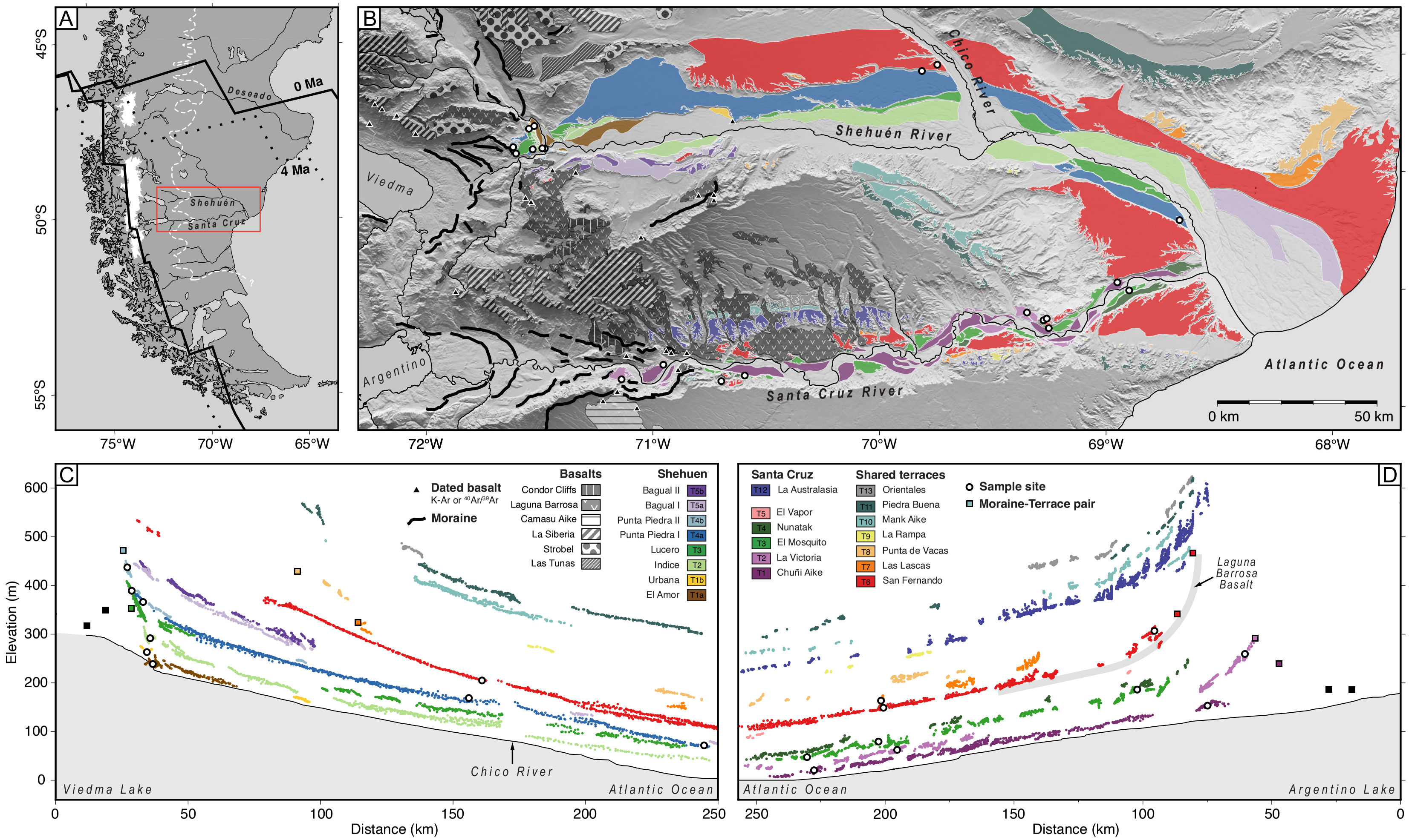
A
B
C
D
45°S
50°S
55°S
75°W
70°W
65°W
0 Ma
4 Ma
Deseado
Shehuén
Santa Cruz
72°W
71°W
70°W
69°W
68°W
49°20'S
49°40'S
50°00'S
50°20'S
Chico River
Shehuén River
Santa Cruz River
Viedma
Argentino
Atlantic Ocean
0 km
50 km
Dated basalt
K-Ar or 40Ar/39Ar
Moraine
Basalts
Condor Cliffs
Laguna Barrosa
Camasu Aike
La Siberia
Strobel
Las Tunas
Shehuen
Bagual II T5b
Bagual I T5a
Punta Piedra II T4b
Punta Piedra I T4a
Lucero T3
Indice T2
Urbana T1b
El Amor T1a
Elevation (m)
Distance (km)
Viedma Lake
Atlantic Ocean
Chico River
Santa Cruz
T12 La Australasia
T5 El Vapor
T4 Nunatak
T3 El Mosquito
T2 La Victoria
T1 Chuñi Aike
Shared terraces
T13 Orientales
T11 Piedra Buena
T10 Mank Aike
T9 La Rampa
T8 Punta de Vacas
T7 Las Lascas
T6 San Fernando
Sample site
Moraine-Terrace pair
Laguna
Barrosa
Basalt
Atlantic Ocean
Argentino Lake

Figure 2. Terrace ages. Black squares = analyzed ages, grey squares = outlier ages. Dashed line = PDE including all samples for terrace, solid line = PDE without outliers.

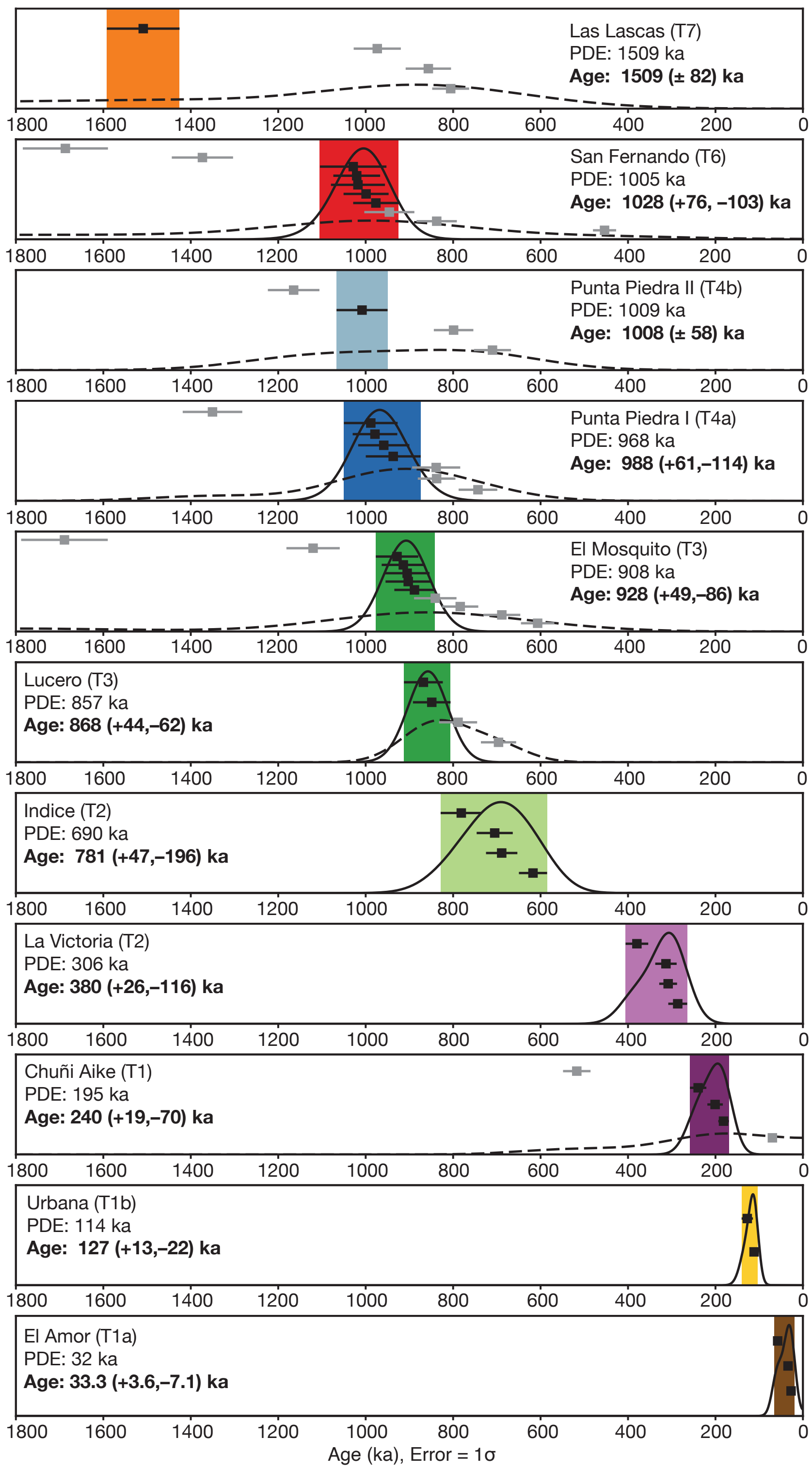

Figure 3. (A) Modeled depth profile and (B) inheritance. (C) Age-elevation plot of Shehuén and (D) Santa Cruz terraces. Dotted lines = uplift rates from Pedoja et al., 2011. Solid grey lines = calculated incision rates (this study). Black squares = interpreted terrace ages, colored bars = age range (Fig. 2). Empty colored squares represent undated terrace levels. Stippled area = dated basalts (Clague et al., 2020).

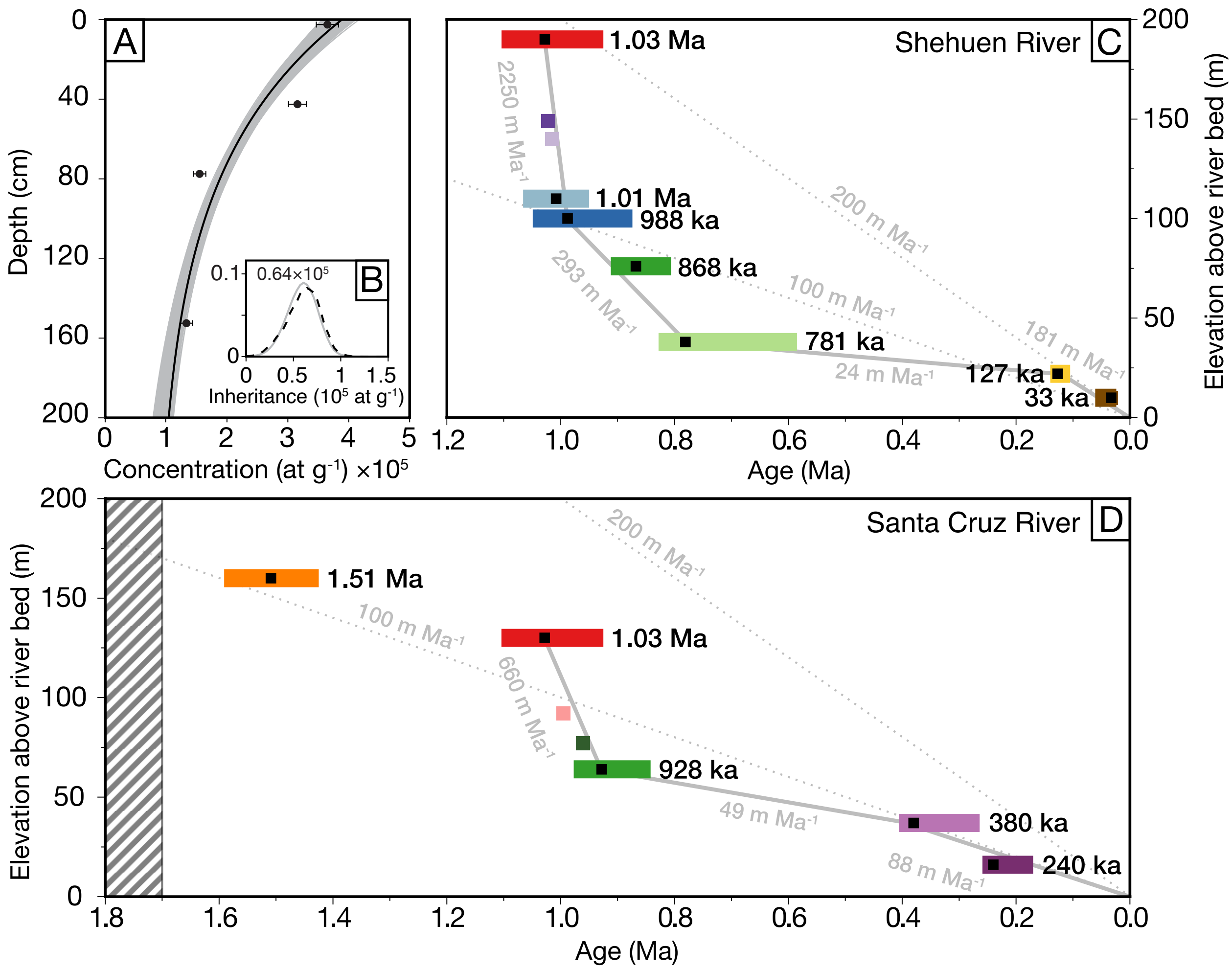

Figure 4. Patagonian glaciations and terrace ages. Top: Age constraints of glaciations in Northern (43–48ºS) and Southern (48–53ºS) Patagonia (see Sup. Mat. for references). Colored bars with black squares = Interpreted terrace ages (Fig. 2). Bottom: ∂^{18}O record from Lisiecki & Raymo, 2005. Numbers identify MIS glaciations associated with terrace formation.

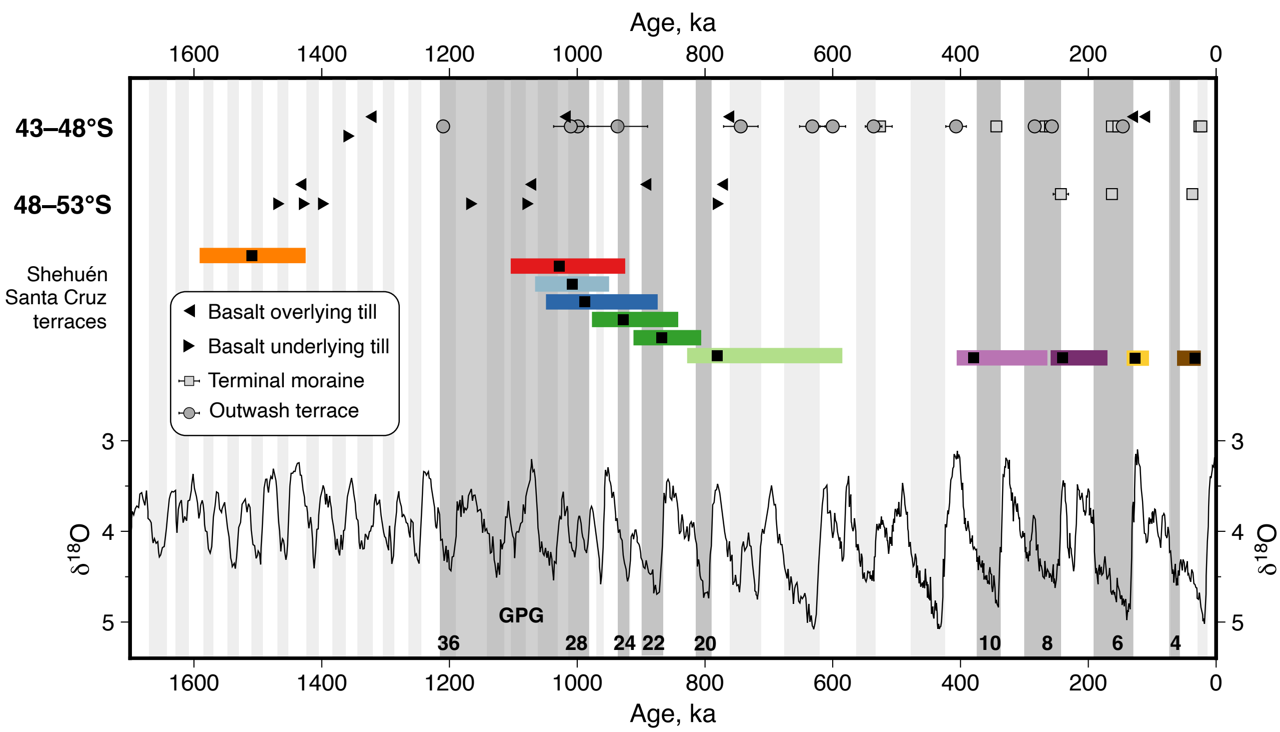

REFERENCES

1. Arnould, M., Coltice, N., Flament, N., Seigneur, V., and Müller, R.D., 2018, On the Scales of Dynamic Topography in Whole-Mantle Convection Models: Geochemistry, Geophysics, Geosystems, v. 19, p. 3140–3163, doi:10.1029/2018gc007516.

2. Ávila, P., and Dávila, F.M., 2020, Lithospheric thinning and dynamic uplift effects during slab window formation, southern Patagonia (45˚-55˚ S): Journal of Geodynamics, v. 133, p. 101689, doi:10.1016/j.jog.2019.101689.

3. Blisniuk, P.M., Stern, L.A., Chamberlain, C.P., Idleman, B., and Zeitler, P.K., 2005, Climatic and ecologic changes during Miocene surface uplift in the Southern Patagonian Andes: Earth and Planetary Science Letters, v. 230, p. 125–142, doi:10.1016/j.epsl.2004.11.015.

4. Clague, J.J., Barendregt, R.W., Menounos, B., Roberts, N.J., Rabassa, J., Martinez, O., Ercolano, B., Corbella, H., and Hemming, S.R., 2020, Pliocene and Early Pleistocene glaciation and landscape evolution on the Patagonian Steppe, Santa Cruz province, Argentina: Quaternary Science Reviews, v. 227, p. 105992, doi:10.1016/j.quascirev.2019.105992.

5. Dávila, F.M., and Lithgow-Bertelloni, C., 2013, Dynamic topography in South America: Journal of South American Earth Sciences, v. 43, p. 127–144, doi:10.1016/j.jsames.2012.12.002.

6. Dietrich, R., Ivins, E.R., Casassa, G., Lange, H., Wendt, J., and Fritsche, M., 2010, Rapid crustal uplift in Patagonia due to enhanced ice loss: Earth and Planetary Science Letters, v. 289, p. 22–29, doi:10.1016/j.epsl.2009.10.021.

7. Gorring, M.L., Kay, S.M., Zeitler, P.K., Ramos, V.A., Rubiolo, D., Fernandez, M.I., and Panza, J.L., 1997, Neogene Patagonian plateau lavas: Continental magmas associated with ridge collision at the Chile Triple Junction: Tectonics, v. 16, p. 1–17, doi:10.1029/96tc03368.

8. Guillaume, B., Martinod, J., Husson, L., Roddaz, M., and Riquelme, R., 2009, Neogene uplift of central eastern Patagonia: Dynamic response to active spreading ridge subduction? Tectonics, v. 28, doi:10.1029/2008tc002324.

9. Griffing, C.Y., Clague, J.J., Barendregt, R.W., Ercolano, B., Corbella, H., Rabassa, J., and Roberts, N.J., 2022, Early and Middle Pleistocene glaciation of the southern Patagonian plain: Journal of South American Earth Sciences, v. 114, p. 103687, doi:10.1016/j.jsames.2021.103687.

10. Hein, A.S., Dunai, T.J., Hulton, N.R.J., and Xu, S., 2011, Exposure dating outwash gravels to determine the age of the greatest Patagonian glaciations: Geology, v. 39, p. 103–106, doi:10.1130/g31215.1.

11. Hollyday, A., Austermann, J., Lloyd, A., Hoggard, M., Richards, F., and Rovere, A., 2023, A Revised Estimate of Early Pliocene Global Mean Sea Level Using Geodynamic Models of the Patagonian Slab Window: Geochemistry, Geophysics, Geosystems, v. 24, doi:10.1029/2022gc010648.

12. Kaplan, M.R., Hein, A.S., Hubbard, A., and Lax, S.M., 2009, Can glacial erosion limit the extent of glaciation? Geomorphology, v. 103, p. 172–179, doi:10.1016/j.geomorph.2008.04.020.

13. Lagabrielle, Y. et al., 2007, Pliocene extensional tectonics in the Eastern Central Patagonian Cordillera: geochronological constraints and new field evidence: Terra Nova, v. 19, p. 413–424, doi:10.1111/j.1365-3121.2007.00766.x.

14. Lagabrielle, Y., Suárez, M., Rossello, E.A., Hérail, G., Martinod, J., Régnier, M., and Cruz, R. de la, 2004, Neogene to Quaternary tectonic evolution of the Patagonian Andes at the latitude of the Chile Triple Junction: Tectonophysics, v. 385, p. 211–241, doi:10.1016/j.tecto.2004.04.023.

15. Lisiecki, L.E., and Raymo, M.E., 2005, A Pliocene-Pleistocene stack of 57 globally distributed benthic δ18O records: Paleoceanography, v. 20, p. n/a-n/a, doi:10.1029/2004pa001071.

16. Mark, H.F., Wiens, D.A., Ivins, E.R., Richter, A., Mansour, W.B., Magnani, M.B., Marderwald, E., Adaros, R., and Barrientos, S., 2022, Lithospheric Erosion in the Patagonian Slab Window, and Implications for Glacial Isostasy: Geophysical Research Letters, v. 49, e2021GL096863, doi:10.1029/2021GL096863.

17. McNab, F., Schildgen, T., Turowski, J.M., & Wickert, A.D., 2023, Diverse responses of alluvial rivers to periodic environmental change: Geophysical Research Letters, v. 50, e2023GL103075. doi.:10.1029/2023GL103075

18. Mercer, J.H., 1983, Cenozoic glaciation in the Southern Hemisphere, Annual Review of Earth and Planetary Sciences, v. 11, p. 99, doi:10.1146/annurev.ea.11.050183.000531.

19. Muller, V.A.P., Sue, C., Valla, P.G., Sternai, P., Simon-Labric, T., Gautheróm, C., Cuffey, K.M., Gurjic, D., Bernet, M., Martinod, J., Ghiglione, M.C., Reiners, P., Willett, C., Shuster, D., Herman, F., Baumgartner, L., and Braun, J., 2024a, Geodynamic and Climatic Forcing

on Late-Cenozoic Exhumation of the Southern Patagonian Andes (Fitz Roy and Torres del Paine massifs): Tectonics, v. 43, doi:10.1029/2023tc007914.

20. Muller, V. A., Sternai, P., and Sue, C., 2024b, Fast uplift in the southern Patagonian Andes due to long-and short-term deglaciation and the asthenospheric window underneath. Solid Earth, v. 15, n. 4, p. 387–404, doi:10.5194/se-15-387-2024
21. Orr, E., Schildgen, T., Tofelde, S., Wittmann, H., and Alonso, R., 2024, Landscape response to tectonic deformation and cyclic climate change since ca. 800 ka in the southern Central Andes: EGUsphere, v. 2024, p. 1–36, doi:10.5194/egusphere-2024-784.
22. Pedoja, K., Regard, V., Husson, L., Martinod, J., Guillaume, B., Fucks, E., Iglesias, M., and Weill, P., 2011, Uplift of quaternary shorelines in eastern Patagonia: Darwin revisited: Geomorphology, v. 127, p. 121–142, doi:10.1016/j.geomorph.2010.08.003.
23. Pico, T., Mitrovica, J.X., Perron, J.T., Ferrier, K.L., and Braun, J., 2019, Influence of glacial isostatic adjustment on river evolution along the U.S. mid-Atlantic coast: Earth and Planetary Science Letters, v. 522, p. 176–185, doi:10.1016/j.epsl.2019.06.026.
24. Pingel, H., Alonso, R.N., Altenberger, U., Cottle, J., and Strecker, M.R., 2019, Miocene to Quaternary basin evolution at the southeastern Andean Plateau (Puna) margin (ca. 24°S lat, Northwestern Argentina): Basin Research, v. 31, p. 808–826, doi:10.1111/bre.12346.
25. Rabassa, J., Coronato, A.M., and Salemme, M., 2005, Chronology of the Late Cenozoic Patagonian glaciations and their correlation with biostratigraphic units of the Pampean region (Argentina): Journal of South American Earth Sciences, v. 20, p. 81–103, doi:10.1016/j.jsames.2005.07.004.

26. Romero, M., Penprase, S. B., Van Wyk de Vries, M. S., Wickert, A. D., Jones, A. G., Marcott, S. A., Strelin, J. A., Martini, M. A., Rittenour, T. M., Brignone, G., Shapley, M. D., Ito, E., MacGregor, K. R., and Caffee, M. W., 2024, Late Quaternary glacial maxima in southern Patagonia: insights from the Lago Argentino glacier lobe: Climate of the Past, v. 20, p. 1861–1883, doi:10.5194/cp-20-1861-2024.

27. Rovere, A., Pappalardo, M., Richiano, S., Aguirre, M., Sandstrom, M.R., Hearty, P.J., Austermann, J., Castellanos, I., and Raymo, M.E., 2020, Higher than present global mean sea level recorded by an Early Pliocene intertidal unit in Patagonia (Argentina): Communications Earth & Environment, v. 1, p. 68, doi:10.1038/s43247-020-00067-6.

28. Rubio-Sandoval, K., Ryan, D.D., Richiano, S., Giachetti, L.M., Hollyday, A., Bright, J., Gowan, E.J., Pappalardo, M., Austermann, J., Kaufman, D.S., and Rovere, A., 2024, Quaternary and Pliocene sea-level changes at Camarones, central Patagonia, Argentina: Quaternary Science Reviews, v. 345, p. 108999, doi:10.1016/j.quascirev.2024.108999.

29. Schellmann, G., 2000, Landscape evolution and glacial history of Southern Patagonia, Argentina, since the late Miocene – some general aspects: Zentrablatt für Geologie und Paläontologie Teil I, p. 1013–1026.

30. Singer, B.S., Ackert, R.P., and Guillou, H., 2004, ^{40}Ar/^{39}Ar and K-Ar chronology of Pleistocene glaciations in Patagonia: GSA Bulletin, v. 116, p. 434–450, doi:10.1130/b25177.1.

31. Strelin, J., and Malagnino, E., 2009, Charles Darwin and the Oldest Glacial Events in Patagonia: The Erratic Blocks of the Río Santa Cruz Valley: Revista de la Asociación Geológica Argentina, v. 64, p. 101–108.

32. Tobal, J.E., Morabito, E.G., Terrizzano, C.M., Zech, R., Colavitto, B., Struck, J., Christl, M., and Ghiglione, M.C., 2021, Quaternary landscape evolution of patagonia at the Chilean Triple Junction: Climate and tectonic forcings: Quaternary Science Reviews, v. 261, p. 106960, doi:10.1016/j.quascirev.2021.106960.

33. Ton-That, T., Singer, B., Mörner, N.A. and Rabassa, J, 1999, Datación de lavas basálticas por $^{40}Ar/^{39}Ar$ y geología glacial de la región del lago Buenos Aires, Provincia de Santa Cruz, Argentina: Revista de la Asociación Geológica Argentina, v. 54, n. 4, p. 333–352.

34. Valla, P., Shuster, D. and van der Beek, P., 2011, Significant increase in relief of the European Alps during mid-Pleistocene glaciations: Nature Geosciences, v. 4, p. 688–692, doi:10.1038/ngeo1242.

35. Wenzens, G., 2000, Pliocene Piedmont Glaciation in the Río Shehuen Valley, Southeast Patagonia, Argentina: Arctic, Antarctic, and Alpine Research, v. 32, p. 46–54, doi:10.1080/15230430.2000.12003338.

SUPPLEMENTAL MATERIAL

Mantle-driven, climatically modulated landscape evolution in Southern Patagonia

Victoria M. Fernandes[1*], Andreas Ruby[1], Fergus McNab[1], Hella Wittmann[1], Andrew D. Wickert[1,2], Lennart Grimm[1] & Taylor Schildgen[1,3]

[1] GFZ German Research Centre for Geosciences, Potsdam, Germany

[2] St. Anthony Falls Laboratory and Department of Earth & Environmental Sciences, University of Minnesota, Minneapolis, USA

[3] Institute for Geosciences, University of Potsdam, Germany

*Corresponding author: milanez@gfz.de

Contents

1) Field photographs

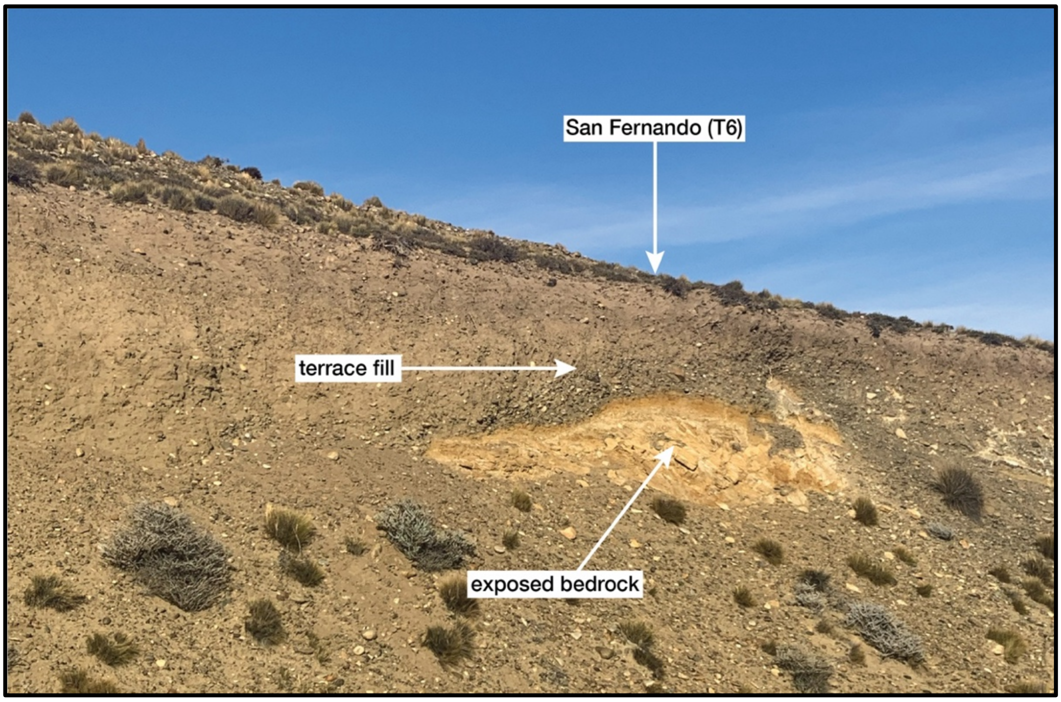

Figure S1. (-68.888036, -49.958265, facing North) Exposure of Miocene bedrock beneath the San Fernando terrace (1028 ka), with terrace fill above it. This bedrocks strath provides evidence that terraces are recording net incision of the landscape.

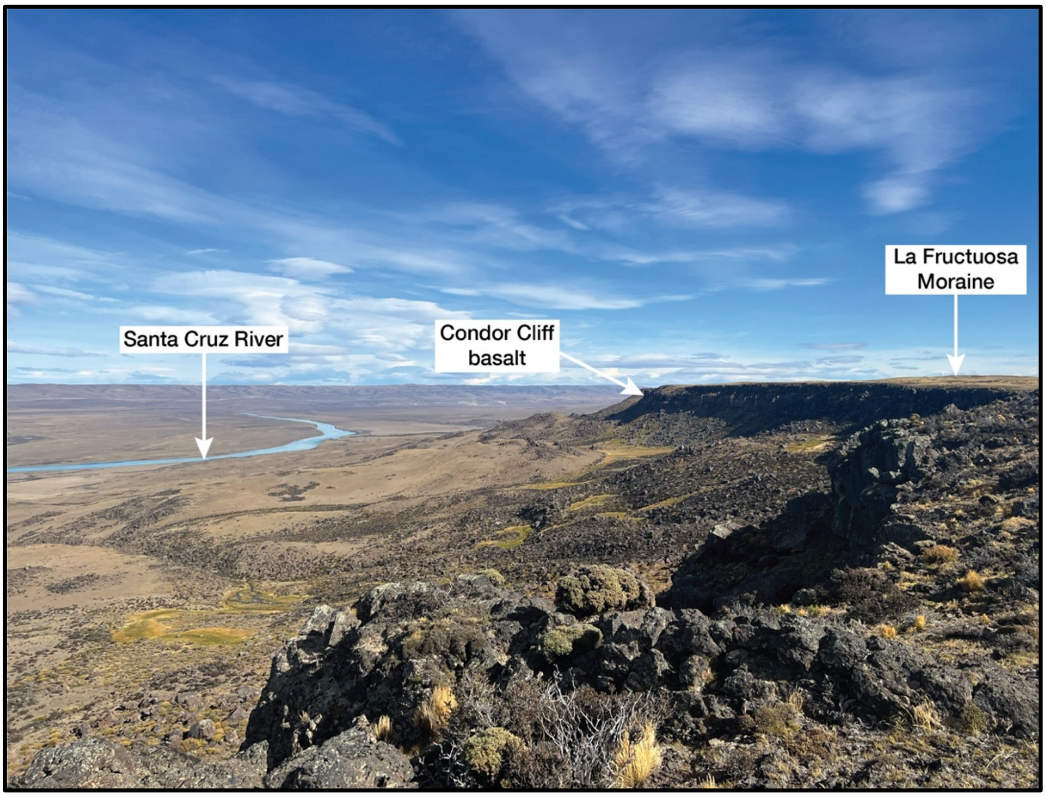

Figure S2. (-70.851314, -50.177535, facing WSW) Geomorphic relationship between basalt flows, overlying glacial and terrace deposits, and the present-day Santa Cruz River. The La Fructuosa Moraine (see Strelin et al. 2009) is geomorphically associated with the San Fernando terrace (1028 ka) and overlies the basalt flows (3.25–1.7 Ma; Clague at al., 2020). Stratigraphic relationships require the terraces to be younger than the basalt flows.

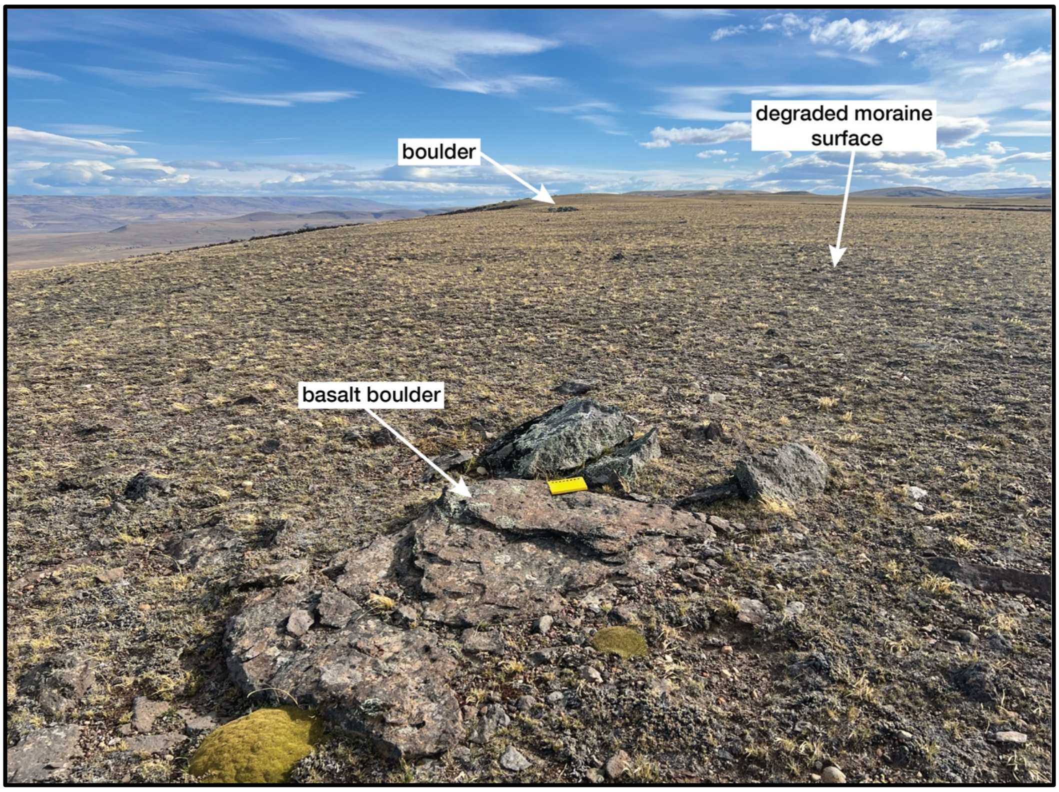

Figure S3. (-70.939393, -50.175788, looking W) Basaltic boulders atop the La Fructuosa moraine, which overlies the basalt flows in the Santa Cruz valley. Incorporation of basaltic boulders into the moraine indicates that glacial deposits postdate the basalt flows (3.25–1.7 Ma; Clague at al., 2020).

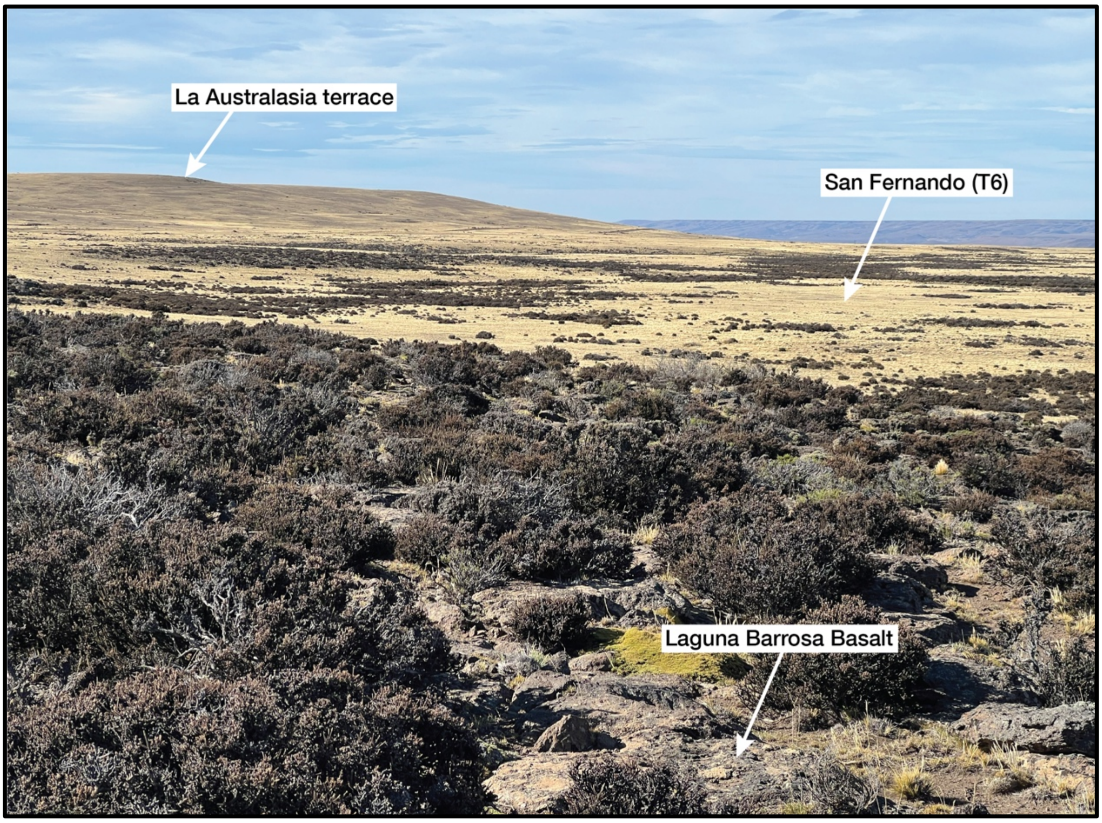

Figure S4. (-70.90705, -50.16204, looking ESE) Geographic relationship between the Condor Cliffs basalts (3.25–1.7 Ma; Clague at al., 2020) and terrace levels. The San Fernando terrace is geomorphically associated with the La Fructuosa moraine.

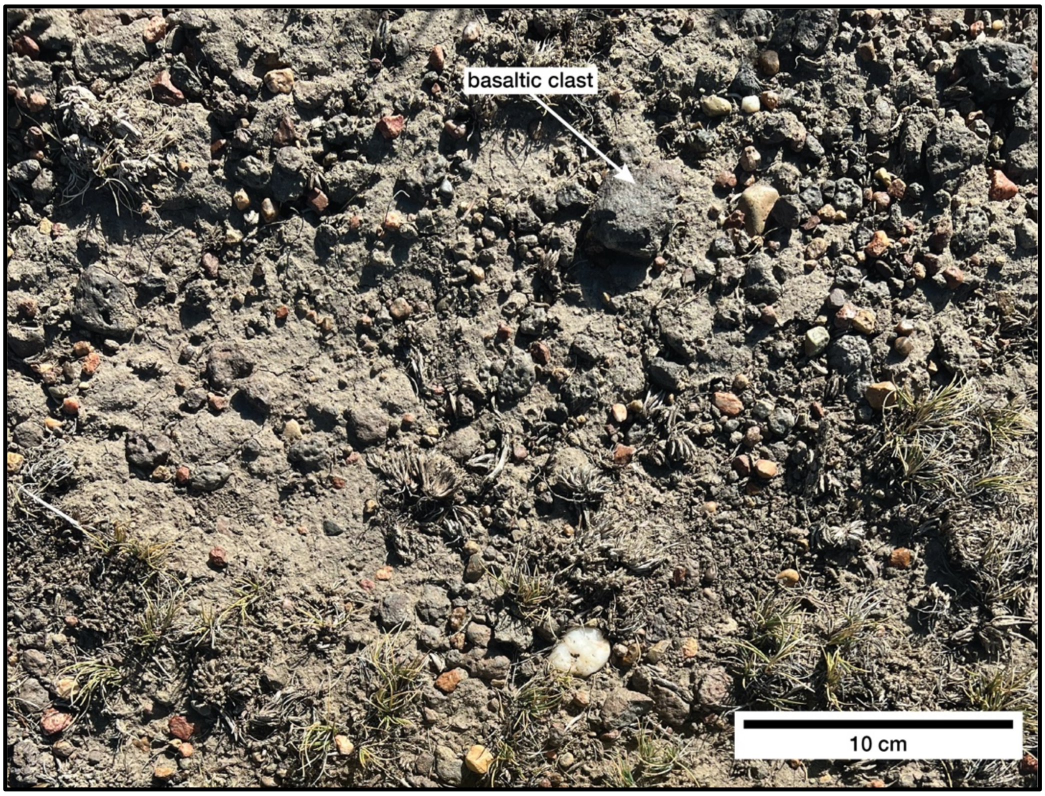

Figure S5. (-70.88781, -50.17072) Surface of the San Fernando terrace (T6), 1028 ka, which lies stratigraphically above the basalt flows. Evidence for presence of basaltic clasts, and thus age relationship, as terrace must have formed after the emplacement of the basalts.

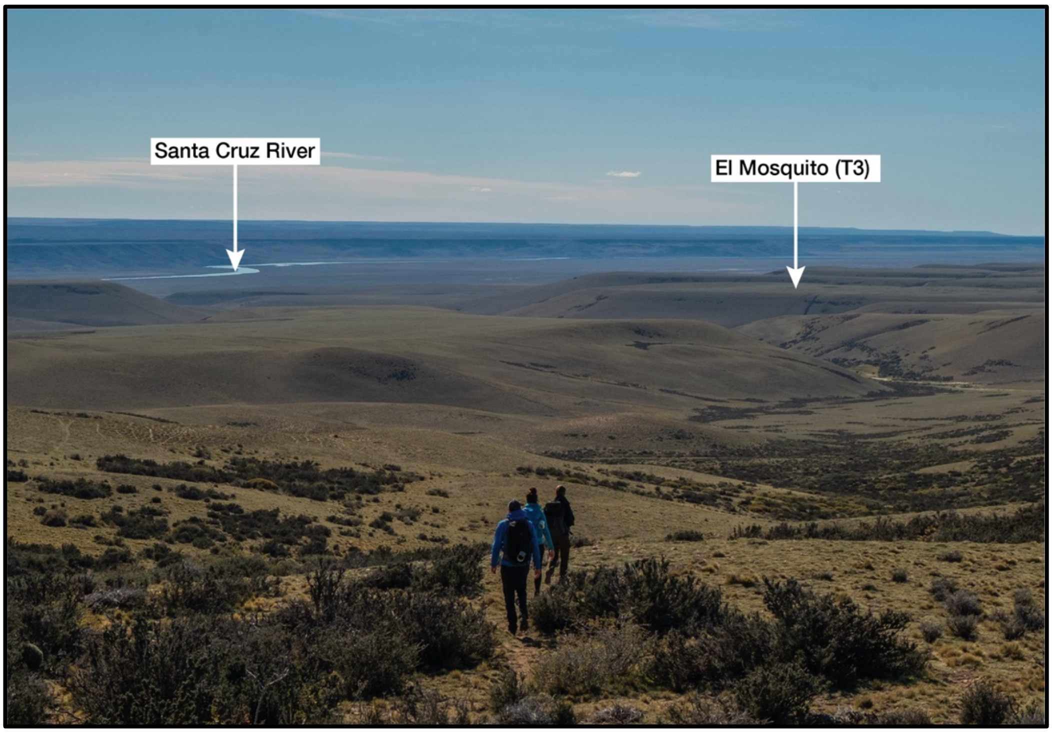

Figure S6. (-70.593857, -50.278610, looking N) View of the Santa Cruz River terraces. Notice the distinctively flat surfaces, which we identify as fluvial terraces.

Figure S7. (-70.594058, -50.245468, looking east. Example terrace surface from the Santa Cruz river showing typical characteristics: flat surfaces, sub-horizontal (or no discernable) dip, 100% exposure (no shielding of cosmic rays), and low vegetation cover.

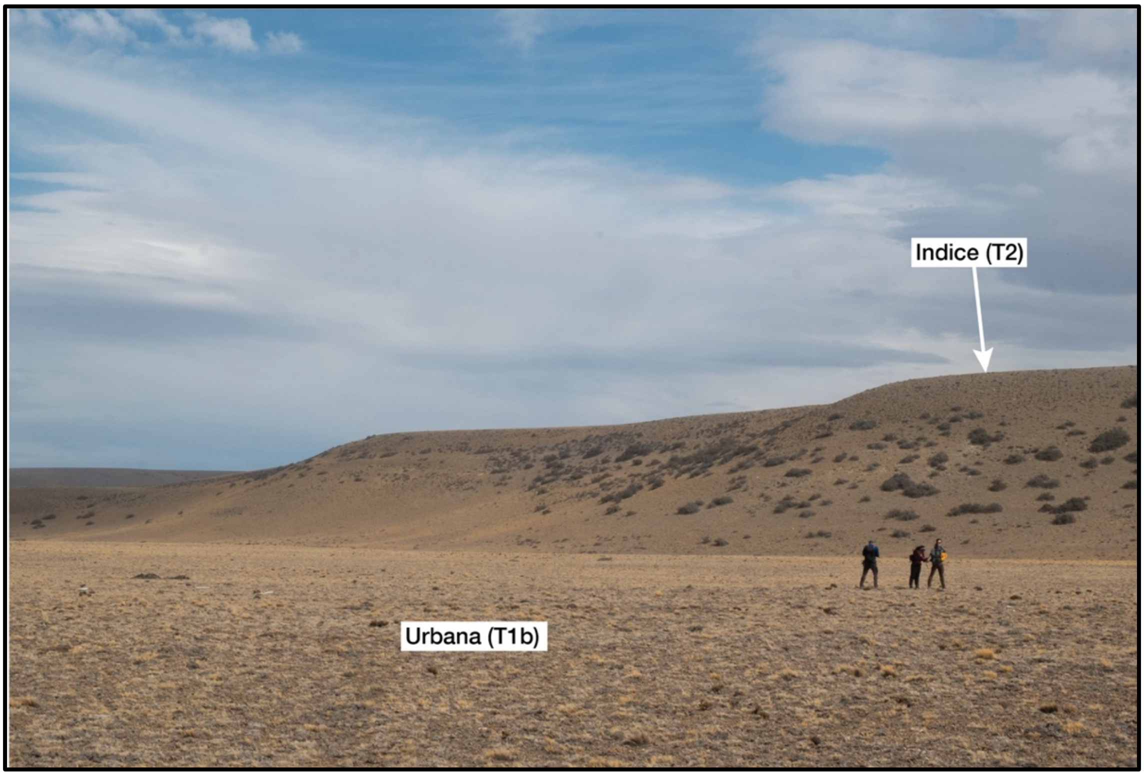

Figure S8. (-71.547152, -49.536721, looking east). Example of terrace riser, with people for scale, near Tres Lagos in the Shehuén river valley. Stratigraphic distinction of terrace levels is aided by prominent, >10 m step in elevation.

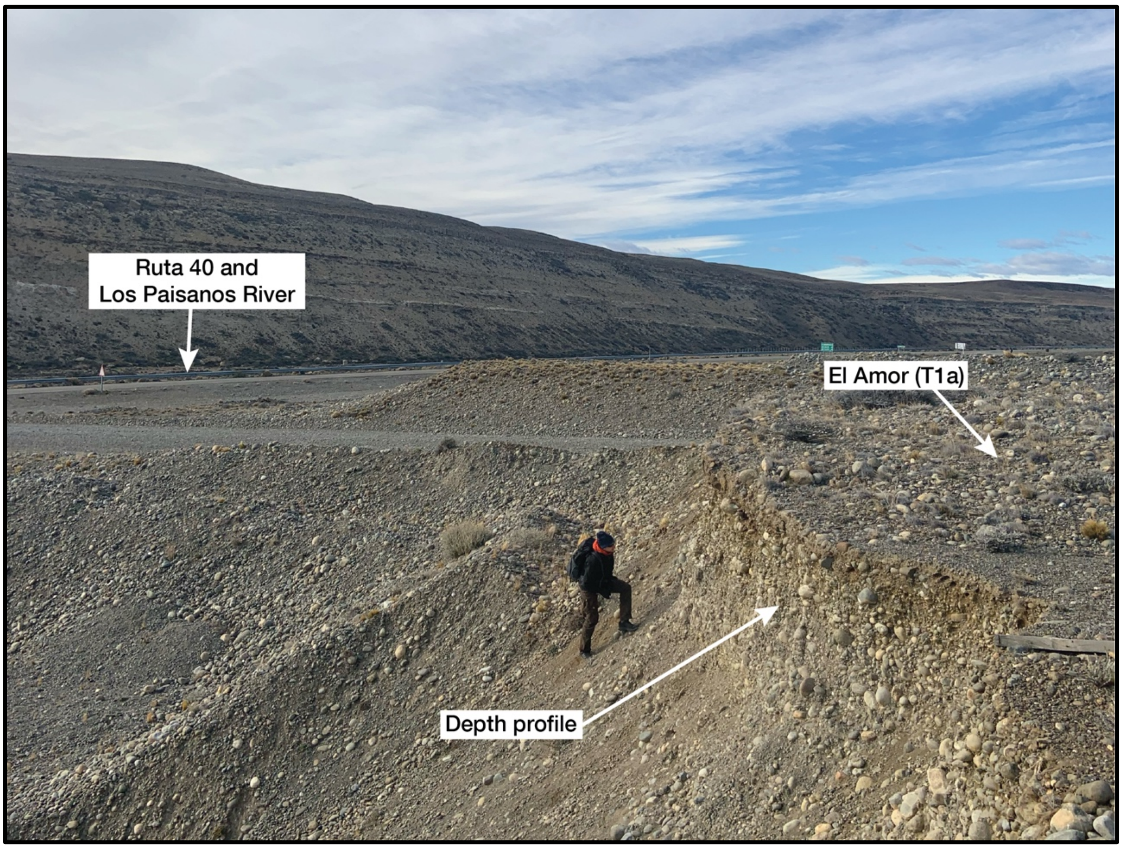

Figure S9. (-71.475482, -49.601076, looking WSW) Location of depth profile near Tres Lagos, Shehuén River.

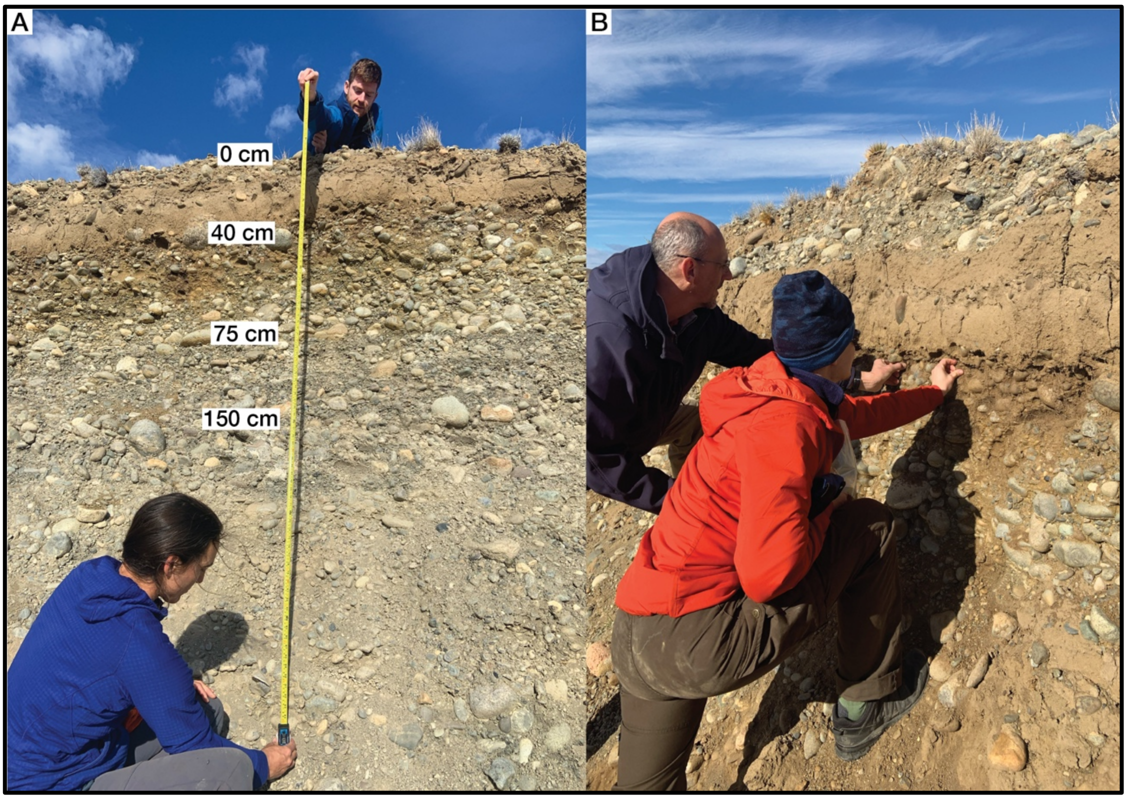

Figure S10. A) Depth profile characteristics, showing depth at which samples were collected. B) Close up of upper portion of the depth profile. Finer sandy material is interpreted as a sand channel within the terrace stratigraphy based on the lenticular shape within the terrace section. The depth profile location was chosen as the location where the upper surface was apparently undisturbed, as it still retains a "desert pavement" of interlocked clasts.

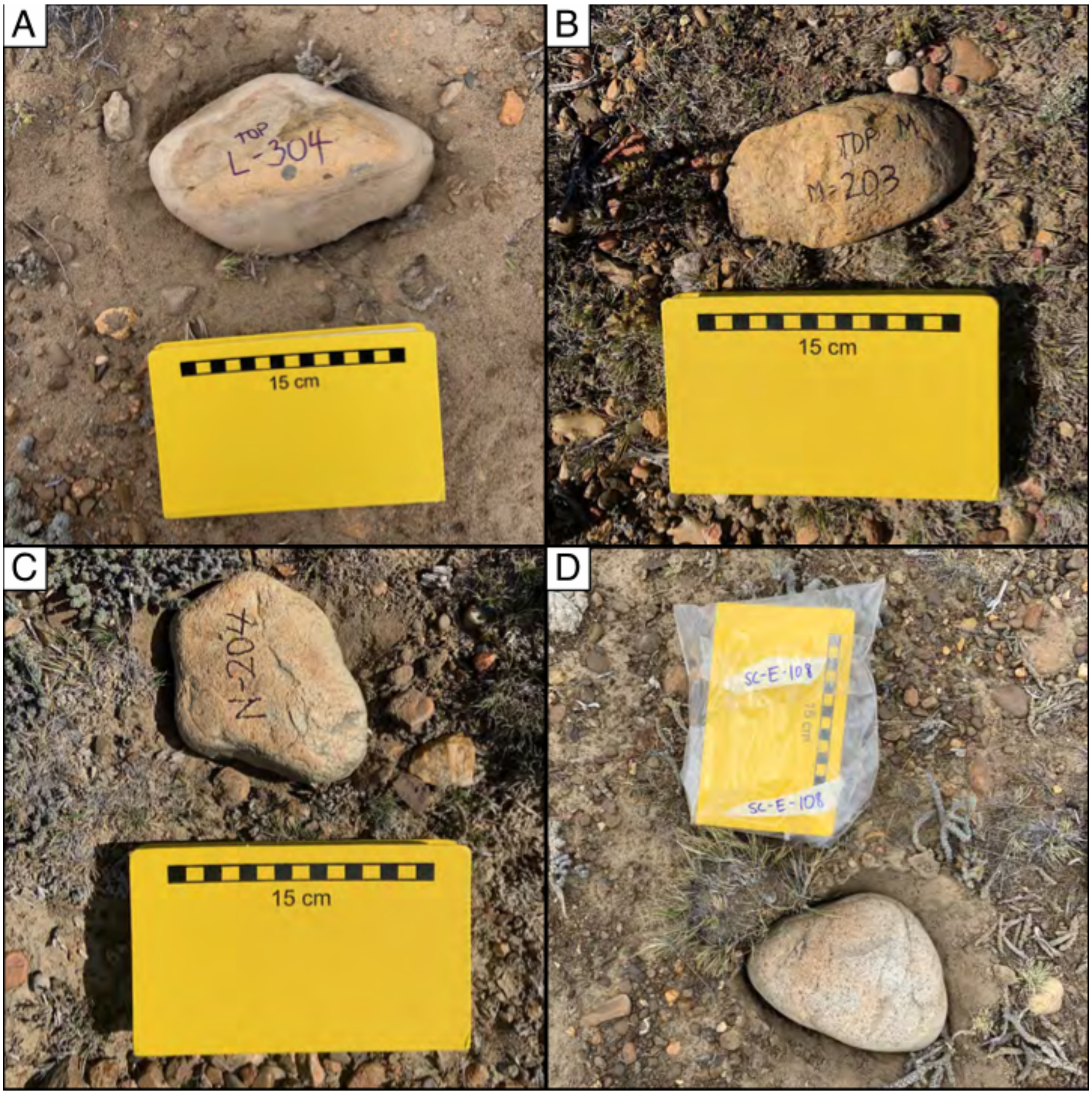

Figure S11. Example cobble samples A) L-304, B)M-203, C) N-204, D) E-108. Samples comprise granitic and quartzitic lithologies, and exhibit smooth, rounded shapes. Cobbles/boulders were clearly embedded in the sediment matrix.

References

1. Clague, J.J., Barendregt, R.W., Menounos, B., Roberts, N.J., Rabassa, J., Martinez, O., Ercolano, B., Corbella, H., and Hemming, S.R., 2020, Pliocene and Early Pleistocene glaciation and landscape evolution on the Patagonian Steppe, Santa Cruz province, Argentina: Quaternary Science Reviews, v. 227, p. 105992, doi:10.1016/j.quascirev.2019.105992.

2) References for mapping moraines, basalt flow and fluvial terraces

Location of glacial moraines in the Argentino-Viedma-San Martín valleys
Mercer et al. (1976), Schellmann (2000), Wenzens (2000), Kaplan et al. (2005), Wenzens (2006), Glasser et al. (2008), Strelin et al. (2009), Glasser et al. (2011), Romero et al. (2024).

Geological maps used for basalts:
Panza et al. (1994), Panza et al. (1998), Panza et al. (2005), Nullo et al. (2006), Cobos et al. (2009), Sacomani et al. (2012), Giacosa et al. (2013), Cobos et al. (2014), Griffing et al. (2020).

Fluvial terrace mapping:
Panza et al. (1994), Panza et al. (1998), Schellmann (2000), Wenzens (2000), Panza et al. (2005), Nullo et al. (2006), Wenzens (2006), Cobos et al. (2009), Strelin et al. (2009), Sacomani et al. (2012), Giacosa et al. (2013), Cobos et al. (2014), Cuitiño et al., (2021), Romero et al. (2024).

References

1. Cobos J., Anselmi, G., Panza, J. L., Giacosa, R. and Escosteguy, L. D., 2009, Hoja Geológica 4972-IV, Tres Lagos, Provincia de Santa Cruz. Programa Nacional de Cartas Geológicas de la República Argentina 1:250.000. Instituto de Geología y Recursos Minerales, Servicio Geológico Minero Argentino, Boletín 340. Buenos Aires.

2. Cobos, J. C., Rodríguez, M. F., and Panza, J. L., 2014, Hoja Geológica 5172-II, Paso Río Bote, Provincia de Santa Cruz. Programa Nacional de Cartas Geológicas de la República Argentina 1:250.000. Instituto de Geología y Recursos Minerales, Servicio Geológico Minero Argentino, Boletín 405. Buenos Aires.

3. Cuitiño, J.I., Raigemborn, M.S., Bargo, M.S., Vizcaíno, S.F., Muñoz, N.A., Kohn, M.J., and Kay, R.F., 2021, Insights on the controls on floodplain-dominated fluvial successions: a perspective from the Early–Middle Miocene Santa Cruz Formation in Río Chalía (Patagonia, Argentina): Journal of the Geological Society, v. 178, p. jgs2020-188, doi:10.1144/jgs2020-188.

4. Giacosa, R., Fracchia, D., Heredia, N., and Pereyra, F., 2013, Hoja Geológica 4972-III, El Chaltén, Provincia de Santa Cruz. Programa Nacional de Cartas Geológicas de la República Argentina 1:250.000. Instituto de Geología y Recursos Minerales, Servicio Geológico Minero Argentino, Boletín 399. Buenos Aires.

5. Glasser, N.F., Jansson, K.N., Harrison, S., and Kleman, J., 2008, The glacial geomorphology and Pleistocene history of South America between 38°S and 56°S: Quaternary Science Reviews, v. 27, p. 365–390, doi:10.1016/j.quascirev.2007.11.011.

6. Glasser, N.F., Jansson, K.N., Goodfellow, B.W., Angelis, H. de, Rodnight, H., and Rood, D.H., 2011, Cosmogenic nuclide exposure ages for moraines in the Lago San Martin Valley, Argentina: Quaternary Research, v. 75, p. 636–646, doi:10.1016/j.yqres.2010.11.005.

7. Griffing, C.Y., Clague, J.J., Barendregt, R.W., Menounos, B., Hemming, S.R., Rabassa, J., Ercolano, B., and Martinez, O., 2021, Pliocene–Pleistocene landscape evolution and watershed reorganization east of the central Andes in Argentine Patagonia (R. B. Waitt, G. D. Thachray, and A. R. Gillespie, Eds.): GSA Special Papers; Untangling the Quaternary Period – A Legacy of Stephen C. Porter, p. 19–35, doi:10.1130/2020.2548(02).

8. Kaplan, M.R., Douglass, D.C., Singer, B.S., Ackert, R.P., and Caffee, M.W., 2005, Cosmogenic nuclide chronology of pre-last glacial maximum moraines at Lago Buenos Aires, 46S, Argentina: Quaternary Research, v. 63, p. 301–315, doi:10.1016/j.yqres.2004.12.003.

9. Mercer, J.H., 1976, Glacial history of Southernmost South America: Quaternary Research, v. 6, p. 125–166, doi:10.1016/0033-5894(76)90047-8.

10. Nullo, F., Blasco, G., Risso, C., Combina, A. and Otamendi, J., 2006, Hoja Geológica 5172-I, El Calafate, Provincia de Santa Cruz. Programa Nacional de Cartas Geológicas de la República Argentina 1:250.000. Instituto de Geología y Recursos Minerales, Servicio Geológico Minero Argentino, Boletín 396. Buenos Aires.

11. Panza, J. L., Irigoyen, M. V., and Genini, A., 1994, Hoja Geológica 4969-IV, Puerto San Julián, Provincia de Santa Cruz. Programa Nacional de Cartas Geológicas de la República Argentina 1:250.000. Instituto de Geología y Recursos Minerales, Servicio Geológico Minero Argentino, Boletín 397. Buenos Aires.

12. Panza, J. L., Marín, G. and Zubía, M.A., 1998, Hoja Geológica 4969-I, Gobernador Gregores, Provincia de Santa Cruz. Programa Nacional de Cartas Geológicas de la República Argentina 1:250.000. Instituto de Geología y Recursos Minerales, Servicio Geológico Minero Argentino, Boletín 239. Buenos Aires.

13. Panza, J. L., Sacomani, L. E. , and Cobos, J. C., 2005, Hoja Geológica 4969-III, Laguna Grande, Provincia de Santa Cruz. Programa Nacional de Cartas Geológicas de la República Argentina 1:250.000. Instituto de Geología y Recursos Minerales, Servicio Geológico Minero Argentino, Boletín 362. Buenos Aires.

14. Romero, M. et al., 2024, Late Quaternary glacial maxima in southern Patagonia: insights from the Lago Argentino glacier lobe: Climate of the Past, v. 20, p. 1861–1883, doi:10.5194/cp-20-1861-2024.

15. Sacomani, L.E., Panza, J. L., Pezzuchi, H., Parisi, C., and Pichersky, G., 2012, Hojas Geológicas 5169-I y 5169-II, Puerto Coig y Puerto Santa Cruz, Provincia de Santa Cruz. Programa Nacional de Cartas Geológicas de la República Argentina 1:250.000. Instituto de Geología y Recursos Minerales, Servicio Geológico Minero Argentino, Boletín 392. Buenos Aires.

16. Schellmann, G., 2000, Landscape evolution and glacial history of Southern Patagonia, Argentina, since the late Miocene – some general aspects: Zentrablatt für Geologie und Paläontologie Teil I, p. 1013–1026.

17. Strelin, J., and Malagnino, E., 2009, Charles Darwin and the Oldest Glacial Events in Patagonia: The Erratic Blocks of the Río Santa Cruz Valley: Revista de la Asociación Geológica Argentina, v. 64, p. 101–108.

18. Wenzens, G., 2000, Pliocene Piedmont Glaciation in the Río Shehuen Valley, Southeast Patagonia, Argentina: Arctic, Antarctic, and Alpine Research, v. 32, p. 46–54, doi:10.1080/15230430.2000.12003338.

19. Wenzens, G., 2006, Terminal Moraines, Outwash Plains, and Lake Terraces in the Vicinity of Lago Cardiel (49S; Patagonia, Argentina) – Evidence for Miocene Andean Foreland Glaciations: Arctic, Antarctic, and Alpine Research, v. 38, p. 276–291, doi:10.1657/1523-0430(2006)38[276:tmopal]2.0.co;2.

3) Extraction of terrace paleo-profiles

Extraction of terrace paleo-profiles was done in four steps: mapping of terraces, sampling of terrace elevations, definition of a projection baseline and point projection. We outline each step in turn.

To quantify the spatial distribution of fluvial terraces, we first conducted a detailed manual mapping of terrace patches above the modern riverbed. Due to the upstream inclination and non-parallel geometry of terrace surfaces relative to the modern river, automatic extraction methods were unsuitable. Particular care was taken to exclude alluvial fans and gully deposits to ensure that mapped polygons represent only the planar terrace treads. Each terrace level was assigned a “Terrace ID” corresponding to their stratigraphic level within the Santa Cruz-Shehuén framework (see Figure S13 for details).

Next, we generated randomly distributed points within each terrace polygon at a fixed-point density. This density-controlled sampling avoided biasing the dataset by over-representing smaller terraces or under-sampling larger ones, although manual addition of points was still necessary in some cases. For each generated point—hereafter referred to as a “terrace point”—we used the QGIS Point Sampling Tool to extract elevation values from the FabDEM dataset and terrace IDs.

Recognizing the sinuous nature of present-day river courses, we opted not to use them directly as projection centerline. Instead, we derived smoothed river centerlines by extracting latitudinal and longitudinal coordinates of the modern river, applying a smoothing algorithm, and resampling the resulting centerline at 5 m intervals. The projection centerline originates at the outlet of the upstream proglacial lakes—Lago Viedma for the Río Shehuén and Lago Argentino for the Río Santa Cruz—and cumulative downstream distances were calculated along this smoothed baseline.

Finally, each terrace point was then orthogonally projected onto this simplified centerline using the GRASS v.distance algorithm, which identifies the nearest centerline coordinate and returns its cumulative downstream distance. We combined these along-channel distances with the corresponding elevations to construct longitudinal terrace profiles. These profiles were subsequently color-coded by terrace ID, consistent with the classification scheme presented in Section 6 and Figure S13.

All the data used to generate the profiles in Figure 1 can be found in Supplementary Dataset 1 (spreadsheet), which contains the Longitude, Latitude, Elevation, Terrace ID and Downstream distance for each terrace point of the Santa Cruz and Shehuén valleys. Additionally, we include the projected present-day river profiles for the Santa Cruz and Shehuén rivers.

4) Depth profile modelling methods and parameters

The depth profile was modelled using the Matlab scheme of Hidy et al. (2010). Results from the depth profile modelling are shown in Figure 10. The values shown on the figure are the Bayesian most probable, with a 2σ error.

Table S1. Simulation Parameters

Location data	Latitude: -49.60019 Longitude: -71.47668 Altitude: 243 masl Strike: 0º Dip: 0º
Topographic/geometric shielding	Factor: 1 Cover: 1
Isotope (^{10}Be)	Half-life: 1.387 Ma % error in half-life: 5
Density data	Does not vary with depth SUD*: 1.6–2.0 g cm^{-3}
Spallogenic Production	Scaling scheme: Lal-Stone time corrected (Stone, 2000 after Lal, 1991) Reference SLHL$^{\varphi}$ Production Rate: 4.03±0.16 at g^{-1} y^{-1} (Kaplan et al., 2011, Location: Puerto Bandera & Hermanita, -50.17011, -72.75087, 240 masl) Constant value: 9.5054 at g^{-1} y^{-1}
Muonic Production	Depth of muon fit: 5 m % error in production rate: 0
Neutron attenuation	SND^{T}: μ =160 g cm^{-2}, σ = 5 g cm^{-2}
Exposure Age	SUD: 0 – 100 ka
Erosion rate	SUD: 0 – 10 mm ka^{-1}
inherited ^{10}Be concentrations	SUD: 0 – $15x10^4$ at g^{-1}
Monte Carlo parameters	Minimization: sum of chi-squared Cutoff chi-squared value: 40 Number of profiles: 100,000

$^{\varphi}$*SLHL = Sea Level High Latitude.* **SUD = Stochastic Uniform Distribution.* ^{T}*SND = Stochastic Normal Distribution*

Table S2. Depth profile sample data

Sample Name	Depth (cm)	$^{10}Be/^{9}Be$	$^{10}Be/^{9}Be$ 1s error (%)	Quartz Mass (g)	Uncorr. ^{10}Be conc. (at/g)	Blank corr. ^{10}Be conc. (at/g)	1s error (at/g)
E-108	0	2.157×10^{-13}	4.2	6.3429	414276	364980	18250
E-104	40	1.711×10^{-13}	4.4	5.8380	325909	315808	9982
E-103	75	7.810×10^{-14}	5.5	5.2263	166334	155051	10298
E-102	150	8.054×10^{-14}	6.5	6.2731	142907	133506	12888

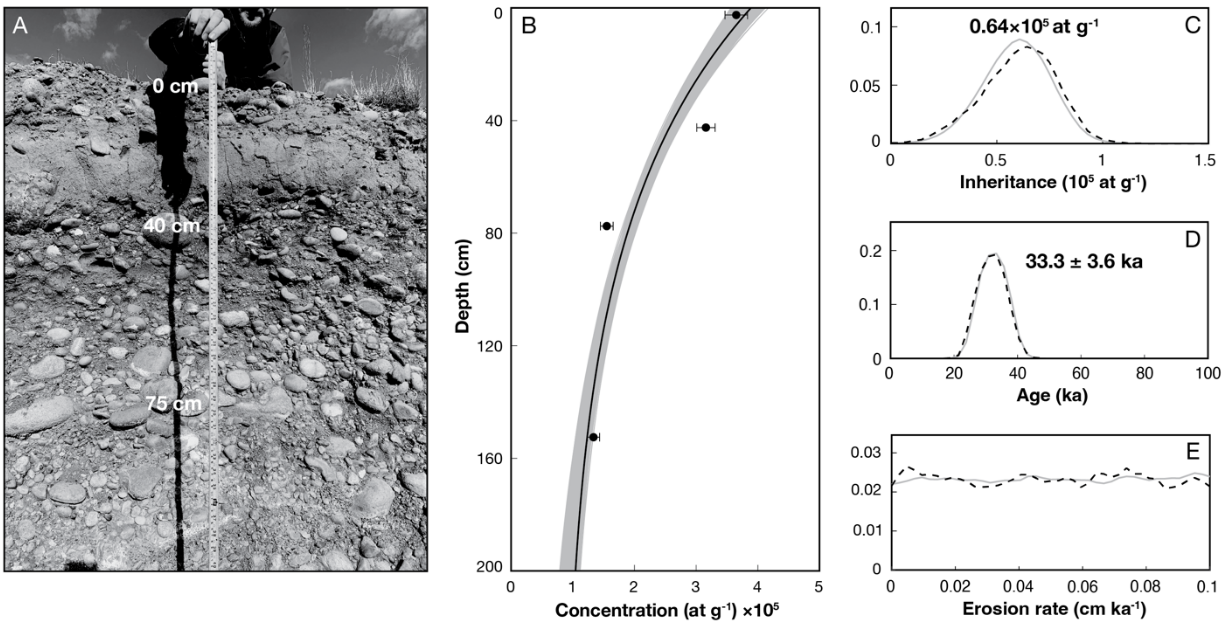

Figure S12. Results of depth profile modeling. (A) Picture showing the terrace cross-section where samples were collected. (B) Concentration versus depth plot. Black line is the 2σ profile solution, and grey lines are best fits. (C) Modeled inheritance. (C) Modeled age. (E) Modeled erosion rate, where grey line shows the probability density function, and dashed black line shows a smoothed minimum χ^2 probability.

Choices for the modelling simulation parameter ranges were made as follows. We assume terrace formation and preservation across moraine-terrace systems in Patagonia are broadly similar, so we guided our parameter choice by those of Hein et al., 2009. For density, we assumed a Stochastic uniform distribution of values between 1.6–2.0 g cm^{-3}. This range is calculated by assuming a general quartz-feldspar grain composition (2.75 g cm^{-3}) with a 25–40% porosity, accounting for the low compaction of the terrace gravels. The stochastic uniform distribution is chosen to not attribute any preference towards any given density, due to the heterogeneity of the material contained within the terrace deposit. For the terrace age, we have an upper limit established by the age range of the overlying terrace level (Urbana, T1b, 127 ± 22 ka). Ages of surface cobbles of the El Amor terrace provided a general guide for the likely terrace age (27–54 ka). We thus assumed a reasonable age range of 0–100 ka. The depth profile modelling of Hein et al. (2009) showed a minimum misfit at an erosion rage of 0.53 mm a^{-1}. Given the lack of evidence for significant surface deflation or sample erosion, as well as reported low boulder erosion rates in other Patagonian sites (Kaplan et al., 2005), we assumed a generally low erosion rate. A choice of 0–10 mm a^{-1} was made to allow for a larger parameter sweep. The maximum possible inherited concentration was taken to be represented by the deepest sample in our section, 13.35 at g^{-1} at 150 cm depth. Thus, a range from 0–15x10^4 at g^{-1} should encompass the range of possible inherited concentrations.

References

1. Hein, A.S., Hulton, N.R.J., Dunai, T.J., Schnabel, C., Kaplan, M.R., Naylor, M. and Xu, S., 2009, Middle Pleistocene glaciation in Patagonia dated by cosmogenic-nuclide measurements on outwash gravels, Earth and Planetary Science Letters, doi:10.1016/j.epsl.2009.06.026

2. Hidy, A.J., Gosse, J.C., Pederson, J.L., Mattern, J.P., and Finkel, R.C., 2010, A geologically constrained Monte Carlo approach to modeling exposure ages from profiles of cosmogenic nuclides: An example from Lees Ferry, Arizona: Geochemistry Geophysics Geosystems, v. 11, Q0AA10, doi:10.1029/2010GC003084.

3. Kaplan, M.R., Strelin, J.A., Schaefer, J.M., Denton, G.H., Finkel, R.C., Schwartz, R., Putnam, A.E., Vandergoes, M.J., Goehring, B.M., and Travis, S.G., 2011, In-situ cosmogenic 10Be production rate at Lago Argentino, Patagonia: Implications for late-glacial climate chronology: Earth and Planetary Science Letters, v. 309, p. 21–32, doi:10.1016/j.epsl.2011.06.018.

4. Lal, D., 1991, Cosmic ray labeling of erosion surfaces: In situ nuclide production rates and erosion models: Earth and Planetary Science Letters, v. 104, p. 424–439, doi:10.1016/0012-821X(91)90220-C.

5. Stone, J.O., 2000, Air pressure and cosmogenic isotope production, Journal f Geophysical Research, v. 105, n. 23, p.753–23, doi:10.1029/2000JB900181.

5) Terrace sample collection and exposure age calculation

We followed a sampling strategy similar the one outlined by Hein et al. (2009), who showed the effectiveness of sampling surface cobbles in the Patagonian steppe. Samples were collected from visibly flat terrace surfaces, away from gullies or scarps, and where access was possible. Sampling surfaces were chosen by their lack of a prominent vegetation, soil or fine sediment cover (see Figure S7). We prioritized sampling cobbles with a dominant quartz lithology (e.g., quartzite or granite), as monomineralic quartz is most resistant to weathering on long timescales. Cobbles were selected based on surface smoothness and lack of evidence for post-depositional weathering or cracking. Our procedure to collect >100 pebbles for each amalgamated pebble sample follows standard sampling of pebbles from individual depth layers within cosmogenic depth profiles. Pebbles with smooth and rounded shapes were selected, as this indicated that they were not recently broken from a larger cobble or boulder (see Figure S11 for examples of sampled clasts). We aimed to collect amalgamated pebble samples and cobble samples at all sites where it was possible. Where it was not possible to collect cobbles, only amalgamated pebble samples were collected.

Samples were crushed whole (small cobbles; < 6 cm) or after cutting to a thickness < 6 cm parallel to the surface. Crushed rock samples were sieved to obtain the 250–500 µm fraction. Cosmogenic ^{10}Be was chemically isolated from pure quartz at GFZ Potsdam, Germany following the protocol of von Blanckenburg et al. (2004). Process blanks (n = 11) and samples were spiked with ca. 165 µg ^{9}Be carrier. ^{10}Be/^{9}Be ratios were measured at the CologneAMS facility (University of Cologne, Germany), normalized to the standards of Nishiizumi et al. (2007), which are consistent with a half-life of ^{10}Be of $1.36 \pm 0.07 \times 10^6$ yr and then converted into ^{10}Be concentrations using ^{9}Be carrier concentrations.

Exposure ages were calculated using the CREp online calculator (Martin et al., 2017; https://crep.otelo.univ-lorraine.fr/#/). The calculator uses the sample thickness and density to standardize the nuclide concentrations of the rock surface. Corrections were made for topographic shielding, but not for vegetation or snow cover, which would be very low to negligible at our semi-arid sampling sites. Topographic shielding for each sample location was initially estimated in the field, and subsequently calculated using the toposhielding functionality in TopotoolBox using an azimuth spacing of 10º and a zenith spacing of 5º (Dunne et al., 1999). For all sample locations, shielding corrections was 0.999 (i.e., full exposure of sample site). Erosion rates were assumed to be zero, based on regional estimates (0–14 mm/ka; Kaplan et al., 2005, Hein et al., 2009). ^{10}Be concentrations were corrected for inheritance based on the value derived from the depth profile (0.64×10^5 at g^{-1}) and average blank concentrations.

Table S3. Exposure age calculation parameters

Nuclide	^{10}Be
Scaling Scheme	Lal-Stone time corrected
Atmosphere model	ERA40
Geomagnetic database	Atmospheric ^{10}Be-based VDM
Production rate	4.03±0.16 at g^{-1} y^{-1} (Kaplan et al., 2011). Location: Puerto Bandera (-50.17011, -72.75087, 240 masl)

Sample details, cosmogenic ^{10}Be concentrations and surface exposure ages (with and without corrections) are reported in the Supplemental Dataset 2.

We find that ages mostly get older (by up to 10%) when using the LSD scaling scheme in the CREp online calculator, rather than the Lal-Stone time corrected scheme. The biggest change is for the oldest ages; younger ages change by only a few percent. When using the Cronus online calculator (version 3) with the same reference production rate, we find that calculated ages are younger, by 4 to 8%, when using the LSDn or Lm scaling scheme. The impact on our discussion and conclusions would be relatively small had we used these alternatively calculated ages: how we correlate some terrace surfaces with MIS stages might change, but the change from high-frequency cycles to 100-kyr cyclicity in the terrace ages would not change, and the calculated incision rates would be only minimally affected (< 10% change). The timing of the change from higher- to lower-frequency forcing also would still correspond to the Mid-Pleistocene Transition.

All the data required for reproducing our ^{10}Be dates are included in the Supplemental Dataset 2 (spreadsheet). There we include general sample information (sample name, terrace and strat level), geolocation (longitude, latitude, elevation and shielding), sample description (sample type, long axis size, thickness, lithology and density), laboratory data ($^{10}Be/^{9}Be$, percent error, quartz mass, carrier mass) and calculated values (^{10}Be concentrations, blank and inheritance corrected ages and all associated errors).

References

1. Dunne, J., Elmore, D., and Muzikar, P., 1999, Scaling factors for the rates of production of cosmogenic nuclides for geometric shielding and attenuation at depth on sloped surfaces: Geomorphology, v. 27, no. 1-2, p. 3-11, doi:10.1016/S0169-555X(98)00086-5.

2. Hein, A.S., Hulton, N.R.J., Dunai, T.J., Schnabel, C., Kaplan, M.R., Naylor, M., and Xu, S., 2009, Middle Pleistocene glaciation in Patagonia dated by cosmogenic-nuclide measurements on outwash gravels: Earth and Planetary Science Letters, v. 286, p. 184–197, doi:10.1016/j.epsl.2009.06.026.

3. Kaplan, M.R., Douglass, D.C., Singer, B.S., Ackert, R.P., and Caffee, M.W., 2005, Cosmogenic nuclide chronology of pre-last glacial maximum moraines at Lago Buenos Aires, 46S, Argentina: Quaternary Research, v. 63, p. 301–315, doi:10.1016/j.yqres.2004.12.003.

4. Kaplan, M.R., Strelin, J.A., Schaefer, J.M., Denton, G.H., Finkel, R.C., Schwartz, R., Putnam, A.E., Vandergoes, M.J., Goehring, B.M., and Travis, S.G., 2011, In-situ cosmogenic 10Be production rate at Lago Argentino, Patagonia: Implications for late-glacial climate chronology: Earth and Planetary Science Letters, v. 309, p. 21–32, doi:10.1016/j.epsl.2011.06.018.

5. Martin, L.C.P., Blard, P.H., Balco, G., Lavé, J., Delunel, R., Lifton, N. and Laurent, V., 2017. The CREp program and the ICE-D production rate calibration database: a fully parameterizable and updated online tool to compute cosmic-ray exposure ages: *Quaternary geochronology*, v. *38*, pp. 25–49, doi:10.1016/j.quageo.2016.11.006.

6. Nishiizumi, K., Imamura, M., Caffee, M.W., Southon, J.R., Finkel, R.C. and McAninch, J., 2007, Absolute calibration of 10Be AMS standards: Nuclear Instruments and Methods in Physics Research Section B: Beam Interactions with Materials and Atoms, v. 258, n. 2, p.403–413, doi:10.1016/j.nimb.2007.01.297.

7. von Blanckenburg, F., Hewawasam, T., and Kubik, P.W., 2004, Cosmogenic nuclide evidence for low weathering and denudation in the wet, tropical highlands of Sri Lanka: Journal of Geophysical Research, v. 109, F03008, doi:10.1029/2003JF000049.

6. Terrace age interpretation

Individual terrace ages are initially stratigraphically constrained, i.e., the interpreted ages must obey the stratigraphic relations established from mapping. Figure S12 shows the interpreted stratigraphic order of all terraces identified in the Shehuén–Santa Cruz system. The stratigraphic position of each terrace was assigned based on its elevation with respect to ones above and below at the Shehuén-Santa Cruz confluence. The basalt flows mark a stratigraphic maximum age for the youngest terraces (T1–T7). The exact stratigraphic relationship between older terraces (T8–T13) and the basalt flows is unclear, and thus we only know that they are older than the lower terraces.

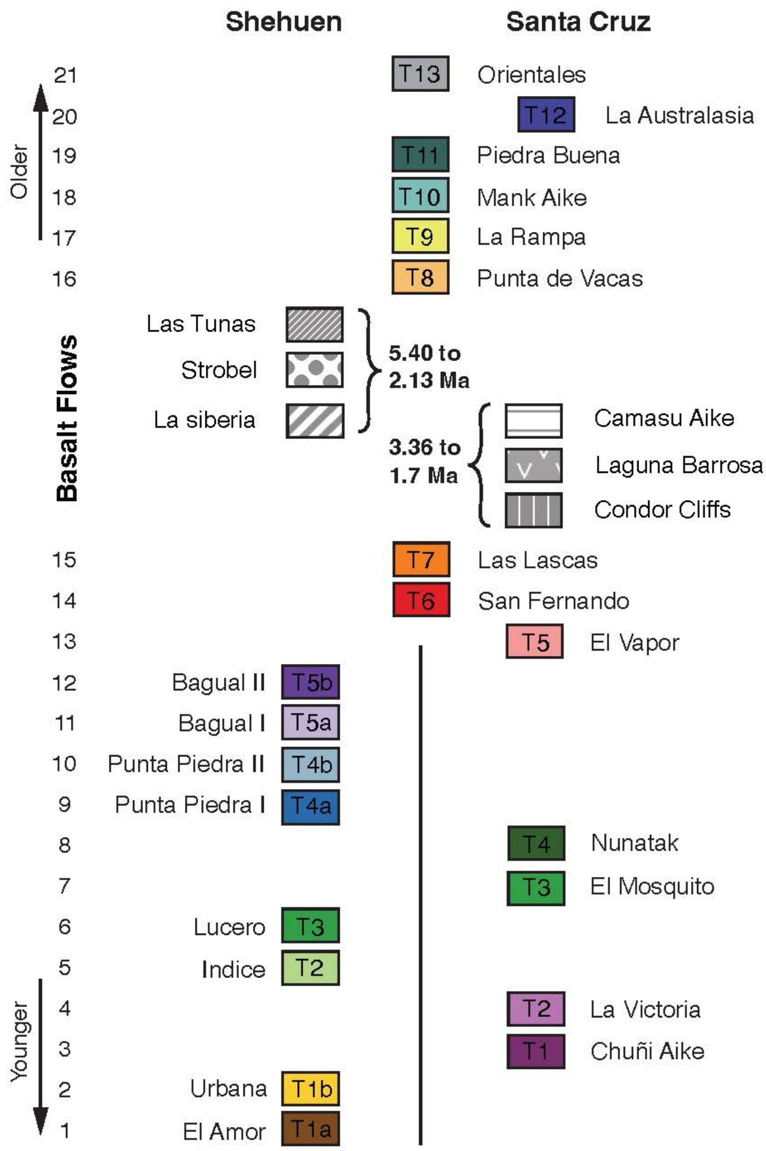

Figure S13. Stratigraphic relations between terraces. Column on the left identifies the terrace level within the entire Shehuén–Santa Cruz system. Terrace identification codes within colored boxes identify the terrace levels within individual fluvial systems. Terrace levels shared by both fluvial systems are located in the center of the diagram.

We interpreted sample ages calculated from ^{10}Be concentrations following blank and inheritance correction. We acknowledge that the latter is simply based on pebble measurements, and may be imperfect when attempting to correct for average inheritance associated with individual cobbles. Nevertheless, we believe that this approach accounts at least for an inheritance associated with the movement of bedload through the river system, which although small, is not negligible, particularly for the youngest surfaces.

We estimated terrace abandonment ages using a probability density estimation (PDE) approach. This method combines individual age distributions, modeled as Gaussian probability density functions based on measured ages and uncertainties, into a composite PDE. Bandwidth estimation was done using Silverman's rule of thumb, where bandwidth, h, is given by

where σ is the standard deviation of the data and *n* is the number of observations (Silverman, 1998). Monte Carlo bootstrapping was employed to quantify uncertainty and compute confidence intervals, while the age of maximum probability was identified as the most likely exposure age ($N = 10^3$). For each terrace level, the most likely abandonment age was estimated twice: once including all ages calculated, and again after outliers were removed, using a Mean Squared Weighted Deviation, to generate a cluster (see dashed and solid lines, respectively, in Figure 2 of main text). Where no cluster was identified, only the PDE including all samples was performed. We define scatter for an age population as the difference between the oldest and youngest age in a group, divided by the oldest age. We calculated the scatter of each age population, before and after removal of outliers.

The probabilistic modeling of the likely exposure ages is used as a guide for interpretation of terrace ages. Old geomorphic surfaces, which commonly exhibit wide exposure age distributions, likely record some component of surface erosion, inflation and/or post-depositional shielding by, for example, snow or loess cover. Data noise generated by these environmental factors, combined with an analytical error, means cosmogenic nuclide ages often have a coarse temporal resolution (10–15% of the absolute age), limiting to how well inheritance/erosion models can estimate the timing of surface abandonment (e.g., Prush & Oskin, 2020, Dortch et al., 2022). The calculated age of pebble samples is indistinguishable from the cobble sample ages, suggesting that amalgamated pebbles can provide useful additional data to the already extensive dataset, and gives us confidence in our results where only amalgamated pebble samples could be collected.

The probabilistic modelling shows that there are statistically coherent, stratigraphically consistent terrace ages across most samples. We take the oldest age within the data cluster as the interpreted terrace age. We assume that post-deposition processes affecting the individual samples (e.g., erosion, transient burial) will lead to an under-estimation of the terrace formation age, whereas we assume that significant inheritance or reworked material from older terraces will generate old outliers. Uncertainty in the interpreted age is taken as the maximum and minimum uncertainty range for ages within a cluster (see colored bands in Figure 2 of main text). Where insufficient terrace ages exist for a strong statistical interpretation of the age (e.g., Punta Piedra II, T4b; Las Lascas, T7), the terrace stratigraphy is used as the primary age constraint. The terrace age and uncertainty are taken from the individual measurement that is stratigraphically consistent with terraces above and below. The age and uncertainty of the youngest terrace is taken from the depth profile modeling, which is consistent with the most likely age from the PDE.

Even if we were to take a different approach and consider that the older ages were reliable, we still must adhere to the stratigraphic order of the terraces, which would mean that the terraces currently interpreted to be between 928 and 1028 ka (Table S4) would shift to a more ill-defined range of around 1100 to 1400 ka. If we assigned these ages to those terrace levels, it would not eliminate the interpreted phase of relatively slow incision, as the lack of terrace preservation between ca. 800 and 400 ka requires minimal net uplift or even subsidence. We prefer the interpretation based on identified age clusters, because we can statistically determine which samples are outliers, and the resulting age clusters agree with the stratigraphic order of the terraces.

Table S4. Interpreted abandonment ages for terraces of the Shehuén (SH) and Santa Cruz (SC) Rivers.

Terrace	Level	System	Age (ka)	Uncertainty (ka)	Min (ka)	N**	Scatter (cluster)	Scatter (all)
*Las Lascas	T7	SC	1509	+82, -82	1427	4(1)	-	47%
San Fernando	T6	SC SH	1028	+76, -103	925	10(5)	5%	73%
*Punta Piedra II	T4b	SH	1008	+58, -58	950	4(1)	-	39%
Punta Piedra I	T4a	SH	988	+61, -114	874	8(4)	5%	45%
El Mosquito	T3	SC	928	+49, -86	842	11(5)	4%	64%
Lucero	T3	SH	868	+44, -62	806	4(2)	2%	20%
Indice	T2	SH	781	+47, -196	585	4(4)	21%	21%
La Victoria	T2	SC	380	+26, -116	264	4(4)	25%	25%
Chuñi Aike	T1	SC	240	+19, -70	170	5(3)	24%	86%
Urbana	T1b	SH	127	+13, -22	105	2(2)	12%	12%
El Amor	T1a	SH	33.3	+3.6, -7.1	24	3(-)	-	43%

* *Indicates terraces where only 1 exposure age was used to interpret the terrace age*
** *Total number of samples (Number of samples in cluster, after outliers were removed)*

References

1. Dortch, J.M., Tomkins, M.D., Saha, S., Murari, M.K., Schoenbohm, L.M., and Curl, D., 2022, A tool for the ages: The Probabilistic Cosmogenic Age Analysis Tool (P-CAAT). Quaternary Geochronology, v. 71, 101323. https://doi.org/10.1016/j.quageo.2022.101323.

2. Prush, V.B., and Oskin, M.E., 2020, A mechanistic erosion model for cosmogenic nuclide inheritance in single-clast exposure ages. Earth and Planetary Science Letters, v. 535, 116066. https://doi.org/10.1016/j.epsl.2020.116066.

3. Silverman, B.W. (1998). Density Estimation for Statistics and Data Analysis (1st ed.). Routledge. https://doi.org/10.1201/9781315140919.

7) Patagonian glacial chronology and correlation with terrace ages

Las Lascas (1509 ± 82 ka)

Since the age of the Las Lascas terrace is only broadly constrained to between 1009–1509 ka, there are multiple large glaciations prior to the Great Patagonian Glaciation (GPG; Mercer, 1976) that could correspond to this terrace. In the Rio Gallegos Valley, 51.5ºS, till deposits overlie a K-Ar dated basalt of 1.47 ± 0.1 Ma, suggesting a minimum age for the glaciation (Mercer, 1976). Till deposits sandwiched between $^{40}Ar/^{39}Ar$ dated basalt flows of 1.43–1.08 Ma at Cerro del Fraile, 50.5ºS, also suggests a glaciation within our age range, but without further constraints (Singer et al., 1999). Glaciogenic deposits interbedded with K-Ar dated basalt flows of 1.36 and 1.32 Ma at Mount Tronador, 41ºS, suggest another possible time frame for the terrace formation (Rabassa et al. 1986). A singular sample of amalgamated quartz pebbles from the Caleufu glacial outwash surface, 40.5ºS, yielded a ^{10}Be exposure age of 1313 ± 37 ka (García Morabito et al., 2021). More exposure ages for this terrace are required to better determine the timing of formation and its correlative glaciation.

San Fernando (1028 +76, -103 ka), Punta Piedra II (1008 ± 58 ka), Punta Piedra I (988 +61, -114 ka)

We interpret these terraces to have been formed by the multiple glaciations associated with the GPG. The timing of onset and end of the GPG is constrained at multiple locations around Patagonia, with evidence for multiple large ice advances occurring within a very short time window. The 1168 ± 14 ka, $^{40}Ar/^{39}Ar$ dated Bella Vista basalt in the Río Gallegos Valley, 52ºS, underlies the most extensive tills in Patagonia and sets a maximum age for the onset of the GPG (Singer et al., 2004). In the moraine and outwash terrace record of Lago Pueyrredón, 47.5ºS, ^{10}Be dated cobbles from the Gorra del Poivre outwash terrace have been used to assign an age to the GPG between 999 ± 28 ka and 1211 ± 36 ka (Hein et al., 2011). Till deposits preserved atop $^{40}Ar/^{39}Ar$ dated basalt flows at Cerro del Fraile, 50.5ºS, record a large glacial advance after 1078 ± 15 ka (Singer et al., 1999). A volcanic flow dated to 1021 ± 102 ka ($^{40}Ar/^{39}Ar$) overlies both the Garganta del Diablo tillite and glacial striations scoured on Cretaceous granites near Mount Tronador, 41ºS, setting a maximum age for one of the GPG glaciations (Rabassa et al., 2005). Near Lago Buenos Aires, 46ºS, the $^{40}Ar/^{39}Ar$ dated Arroyo Telken basalt flow overlies till deposits, suggesting the GPG glaciation is no older than 1016 ± 10 ka (Ton-That et al., 1999, Singer et al., 2004). Finally, the T3 terrace of the Deseado River, 46.5ºS, has a loosely constrained ^{10}Be derived exposure age of 1010 ± 27 ka (Tobal et al. 2021). The three additional terraces between the T3 terrace and the next dated surface at 937 ± 33 ka within the Deseado River (Tobal et al., 2021) corroborates the evidence that the GPG comprised multiple large glaciations (MIS 36–28, 1215–982 ka).

El Mosquito (928 +49, -86 ka)

The El Mosquito terrace can be correlated to the Bella Vista outwash gravels, 52ºS, which are capped by a 890 ka, $^{40}Ar/^{39}Ar$ dated basalt flow (Griffing et al., 2022). The T7 terrace of the Deseado River, with a 937 ± 33 ka ^{10}Be derived exposure age, was also likely abandoned at the same period (Tobal et al. 2021). We correlate this terrace to the end of MIS 24 (936 ka).

Lucero (868 +44, -62 ka)

To our knowledge, there are no other records of large-scale glaciations that can be correlated to the age of the Lucero terrace. We thus interpret it as evidence for a large glaciation during MIS 22 (900 ka), with the terrace abandonment and incision during the subsequent interglacial.

Indice (781 +47, -196 ka)

The ^{10}Be exposure age of the T8 terrace from the Deseado River, 47ºS, is broadly constrained to 744 ± 20 ka (Tobal et al., 2021). Magnetically normally polarized tills and glacial deposits exposed along the coast near Río Gallegos, 52.5ºS, suggests extensive glaciations also occurred after 774 ka (Bruhnes Chron), but not younger than 450 ka, based on ^{40}Ar/^{39}Ar dated basalts that overlie the deposits (Griffing et al. 2022). We correlate this terrace with the end of MIS 20 (814 ka).

La Victoria (380 +26, -118 ka)

The ^{40}Ar/^{39}Ar dated, 760 ± 14 ka Arroyo Page basalt overlies the Telken moraines of Lago Buenos Aires, 46.5ºS, suggesting a minimum age of glaciation (Ton-That et al. 1999, Singer et al., 2004). The age of the La Victoria terrace can be correlated to the 474–411 ka, (^{10}Be exposure age) terrace and outwash plain of the upstream Deseado River, 46ºS, although this age is only constrained by 2 dated samples (Tobal et al., 2021). At Lago Buenos Aires, 46ºS, the Moreno III moraine has a ^{10}Be exposure age of 344 ± 8 ka (Kaplan et al., 2005). Dated cobbles and pebbles from this study are 4 km downstream of, and geographically associated with the Arroyo Verde I moraine (Romero et al., 2024), which has a single ^{10}Be derived exposure age of 243 ± 12 ka from a boulder surface. It is likely that this younger moraine age is due to surface deflation, as seen for outwash terrace–moraine pairs near Lago Buenos Aires (Hein et al., 2009). We correlate the La Victoria terrace to the end of MIS 10 (337 ka).

Chuñi Aike (240 +19, -70 ka)

There are several sites where landforms have ages similar to the Chuñi Aike terrace: (1) ^{10}Be derived 267 ± 9 ka moraines of the Ñirehuao glacier, 45ºS (Peltier et al., 2023), (2) a 260 ± 7 ka outwash gravel surface in Lago Pueyrredón, 47.5ºS, based on ^{10}Be depth profile modelling (Hein et al., 2009), and (3) the ^{10}Be derived 257 ± 7 ka Outwash Terrace I of the Corcovado River, 43.5ºS (Leger et al., 2023). ^{10}Be exposure ages of moraines and outwash terraces of the Moreno system in Lago Buenos Aires, 46.5ºS, constrain a glaciation to 260–270 ka (Hein et al., 2017, Cogez et al., 2018). The Chuñi Aike terrace is geomorphically equivalent to the Arroyo Verde II moraine in the Lago Argentino sequence, in which boulders have reported exposure ages of 163 ± 8 ka (Romero et al., 2024). As with the Arroyo Verde I–La Victoria terrace pair, it is likely that the younger moraine boulder ages are an artifact of deflation/boulder displacement (see, e.g., Hein et al., 2009). We assign the timing of terrace formation to the end of MIS 8 (243 ka).

Urbana (127 +13, -22 ka)

Several ^{10}Be exposure ages of moraines and outwash terraces are in agreement with the Urbana terrace age: (1) the 146 ± 4 ka moraine of the Ñirehuao glacier, 45ºS (Peltier et al., 2023), (2) the 146 ± 5 ka Moreno I moraine of Lago Buenos Aires, 46ºS (Kaplan et al., 2005), and (3) the 146 ± 4 ka Río Corcovado II outwash terrace (Leger et al., 2023). Immediately upstream of the terrace deposits, in the Lago San Martín moraine sequence, the M5 moraine has a ^{10}Be exposure age of 99 ± 11 ka, albeit with only 2 boulder samples (Glasser et al., 2011). Near Lago Buenos Aires, the Cerro Volcán basalt, ^{40}Ar/^{39}Ar dated to 109 ± 4 ka, overlies a an outwash gravel surfaces that grade to the Moreno moraines, setting a minimum age for the glaciation (Singer et al., 2004). The evidence suggests the terrace formed at the end of MIS 6 (130 ka).

El Amor (33 +3.6, -7.1 ka)

The terrace is geographically associated with the M3 moraine of Lago San Martín, located 65 km upstream of the depth profile in this study, with a reported ^{10}Be exposure age of 34.4 ± 3 ka (Glasser et al., 2011). It is also well correlated with the ^{10}Be exposure dated 37 ± 1 ka El Tranquilo II moraine of the Lago Argentino moraine sequences (Romero et al., 2024). We correlate this terrace to late MIS 3 (29–57 ka) glacial expansions.

Other regional glaciations

There is evidence for glaciations in the region to which our dated terraces do not correlate. These are mostly located in Northern Patagonia (43–48ºS; see Figure 4). The Deseado I outwash of Lago Buenos Aires has a ^{10}Be exposure age (recalculated with CREP) of 454 ± 39 ka and is assigned to MIS 12, while the oldest age for the Deseado II outwash is 536 ± 13 ka, and assigned to MIS 16. An MIS 16 glaciation is further evidenced by a 526 ± 19 ka ^{10}Be age for the Deseado II moraine (Tobal et al., 2021). A 600 ± 20 ka ^{10}Be age for the Intermediate Caracoles outwash cobbles from Lago Pueyrredón, also assigned to MIS 16 (Hein et al., 2011). There are no currently dated terraces in the Santa Cruz or Shehuén Rivers that can be correlated to these glaciations.

References

1. Cogez, A., Herman, F., Pelt, É., Reuschlé, T., Morvan, G., Darvill, C., M., Norton, K., P., Christl, M., Märki, L., and Chabaux, F., 2018, U–Th and ^{10}Be constraints on sediment recycling in proglacial settings, Lago Buenos Aires, Patagonia: Earth Surface Dynamics, v. 6, p. 121–140, doi:10.5194/esurf-6-121-2018

2. García Morabito, E., Beltrán-Triviño, A., Terrizzano, C.M., Bechis, F., Likerman, J., Quadt, A.V., and Ramos, V.A., 2021, The Influence of Climate on the Dynamics of Mountain Building Within the Northern Patagonian Andes: Tectonics, v. 40, doi:10.1029/2020tc006374.

3. Glasser, N.F., Jansson, K.N., Goodfellow, B.W., Angelis, H. de, Rodnight, H., and Rood, D.H., 2011, Cosmogenic nuclide exposure ages for moraines in the Lago San Martin Valley, Argentina: Quaternary Research, v. 75, p. 636–646, doi:10.1016/j.yqres.2010.11.005.

4. Griffing, C.Y., Clague, J.J., Barendregt, R.W., Ercolano, B., Corbella, H., Rabassa, J., and Roberts, N.J., 2022, Early and Middle Pleistocene glaciation of the southern Patagonian plain: Journal of South American Earth Sciences, v. 114, p. 103687, doi:10.1016/j.jsames.2021.103687.

5. Hein, A.S., Hulton, N.R.J., Dunai, T.J., Schnabel, C., Kaplan, M.R., Naylor, M., and Xu, S., 2009, Middle Pleistocene glaciation in Patagonia dated by cosmogenic-nuclide measurements on outwash gravels: Earth and Planetary Science Letters, v. 286, p. 184–197, doi:10.1016/j.epsl.2009.06.026.

6. Hein, A.S., Dunai, T.J., Hulton, N.R.J., and Xu, S., 2011, Exposure dating outwash gravels to determine the age of the greatest Patagonian glaciations: Geology, v. 39, p. 103–106, doi:10.1130/g31215.1.

7. Hein, A.S., Cogez, A., Darvill, C.M., Mendelova, M., Kaplan, M.R., Herman, F., Dunai, T.J., Norton, K., Xu, S., Christl, M., and Rodés, Á., 2017, Regional mid-Pleistocene glaciation in

central Patagonia: Quaternary Science Reviews, v. 164, p. 77–94, doi:10.1016/j.quascirev.2017.03.023.

8. Kaplan, M.R., Douglass, D.C., Singer, B.S., Ackert, R.P., and Caffee, M.W., 2005, Cosmogenic nuclide chronology of pre-last glacial maximum moraines at Lago Buenos Aires, 46S, Argentina: Quaternary Research, v. 63, p. 301–315, doi:10.1016/j.yqres.2004.12.003.

9. Leger, T.P.M., Hein, A.S., Rodés, Á., Bingham, R.G., Schimmelpfennig, I., Fabel, D., Tapia, P., and Team, A., 2023, A cosmogenic nuclide-derived chronology of pre-Last Glacial Cycle glaciations during MIS 8 and MIS 6 in northern Patagonia: Climate of the Past, v. 19, p. 35–39, doi:10.5194/cp-19-35-2023.

10. Mercer, J.H., 1976, Glacial history of Southernmost South America: Quaternary Research, v. 6, p. 125–166, doi:10.1016/0033-5894(76)90047-8.

11. Peltier, C., Kaplan, M.R., Sagredo, E.A., Moreno, P.I., Araos, J., Birkel, S.D., Villa-Martínez, R., Schwartz, R., Reynhout, S.A., and Schaefer, J.M., 2023, The last two glacial cycles in central Patagonia: A precise record from the Ñirehuao glacier lobe: Quaternary Science Reviews, v. 304, p. 107873, doi:10.1016/j.quascirev.2022.107873.

12. Rabassa, J., Evenson, E. and Stephens, G., 1986, Nuevas evidencias del englazamiento Piioceno-Pleistoceno Inferior en los Andes Patagónicos Septentrionales: Gerro Tronador, Rio Negro: Asociación Geológica Argentina Rev., v. 41, n. 3-4, p. 405–409.

13. Rabassa, J., Coronato, A.M., and Salemme, M., 2005, Chronology of the Late Cenozoic Patagonian glaciations and their correlation with biostratigraphic units of the Pampean region (Argentina): Journal of South American Earth Sciences, v. 20, p. 81–103, doi:10.1016/j.jsames.2005.07.004.

14. Romero, M. et al., 2024, Late Quaternary glacial maxima in southern Patagonia: insights from the Lago Argentino glacier lobe: Climate of the Past, v. 20, p. 1861–1883, doi:10.5194/cp-20-1861-2024.

15. Singer, B.S., Hoffman, K.A., Chauvin, A., Coe, R.S., and Pringle, M.S., 1999, Dating transitionally magnetized lavas of the late Matuyama Chron: Toward a new $^{40}Ar/^{39}Ar$ timescale of reversals and events: Journal of Geophysical Research: Solid Earth, v. 104, p. 679–693, doi:10.1029/1998jb900016.

16. Singer, B.S., Ackert, R.P., and Guillou, H., 2004, $^{40}Ar/^{39}Ar$ and K-Ar chronology of Pleistocene glaciations in Patagonia: GSA Bulletin, v. 116, p. 434–450, doi:10.1130/b25177.1.

17. Tobal, J.E., Morabito, E.G., Terrizzano, C.M., Zech, R., Colavitto, B., Struck, J., Christl, M., and Ghiglione, M.C., 2021, Quaternary landscape evolution of patagonia at the Chilean Triple Junction: Climate and tectonic forcings: Quaternary Science Reviews, v. 261, p. 106960, doi:10.1016/j.quascirev.2021.106960.

18. Ton-That, T., Singer, B., Mörner, N.-A., and Rabassa, J., 1999, Datación de lavas basálticas por $^{40}Ar/^{39}Ar$ y geología glacial de la región del lago Buenos Aires, provincia de Santa Cruz, Argentina: Revista de la Asociación Geológica Argentina, v. 54, p. 333–352.

8) Uplift Calculations for heated asthenosphere

Here we assess how the emplacement of hot asthenospheric material at the base of the lithosphere could generate isostatic uplift. We use the equations (and code) outlined by Fernandes et al., 2024. Assuming isostasy prevails, uplift relative to reference mantle (U) can be calculated as

$$U = \frac{h\alpha\Delta T_p}{1 - \alpha T_p^o} \quad (1)$$

Where h is the thickness of the hot asthenospheric layer which sits beneath the lithosphere, thermal expansivity α = 3.3 x 10^{-5} K^{-1}, T_p^o = 1333 ºC is the reference background potential temperature, and ΔT_p is the excess potential temperature. Uplift is calculated as a function of potential temperature rather than absolute temperature because the latter varies as function of depth (strictly pressure), and we are interested in isolating contributions from thermal anomalies.

We assume that the emplacement of hot asthenospheric material beneath the lithosphere is within a layer of thickness h = 200 km, as suggested by the depth of low shear-wave velocity anomalies beneath the slab window (Mark et al., 2022). An excess mantle potential temperature of 150–200ºC is estimated from geodynamic thermo-mechanical modelling of GNSS-derived surface uplift rates in Patagonia (Muller et al., 2024). Placing these values into equation 1 gives a predicted uplift of 1.03–1.38 km.

References

1. Fernandes, V.M., Roberts, G.G., and Richards, F., 2024, Testing Mantle Convection Simulations with Paleobiology and Other Stratigraphic Observations: Examples from Western North America: Geochemistry, Geophysics, Geosystems, v. 25, p. e2023GC011381, doi:10.1029/2023gc011381.

2. Mark, H.F., Wiens, D.A., Ivins, E.R., Richter, A., Mansour, W.B., Magnani, M.B., Marderwald, E., Adaros, R., and Barrientos, S., 2022, Lithospheric Erosion in the Patagonian Slab Window, and Implications for Glacial Isostasy: Geophysical Research Letters, v. 49, doi:10.1029/2021gl096863.

3. Muller, V.A.P., Sternai, P., and Sue, C., 2024, Fast uplift in the southern Patagonian Andes due to long- and short-term deglaciation and the asthenospheric window underneath: Solid Earth, v. 15, p. 387–404, doi:10.5194/se-15-387-2024.